AGU PUBLICATIONS

JGR

Journal of Geophysical Research: Oceans

RESEARCH ARTICLE

10.1002/2016JC012471

This article is a companion to *Taskjelle et al.* [2017a], doi:10.1002/2016JC012187.

Special Section:
Atmosphere-ice-ocean-ecosystem Processes in a Thinner Arctic Sea Ice Regime: the Norwegian Young Sea ICE Cruise 2015 (N-ICE2015)

Key Points:
- Absorption and especially scattering in the water column significantly increased during an Arctic under-ice bloom of *Phaeocystis pouchetii*
- The ratio between estimated scalar (spherical) and estimated downwelling planar irradiance (400–700 nm) reached 1.85 under snow-covered ice
- The bloom increased light availability (400–700 nm) at ice-ocean interface due to high scattering in the underlying water column

Correspondence to:
A. K. Pavlov,
alexey.pavlov@npolar.no

Citation:
Pavlov, A. K., T. Taskjelle, H. M. Kauko, B. Hamre, S. R. Hudson, P. Assmy, P. Duarte, M. Fernández-Méndez, C. J. Mundy, and M. A. Granskog (2017), Altered inherent optical properties and estimates of the underwater light field during an Arctic under-ice bloom of *Phaeocystis pouchetii*, *J. Geophys. Res. Oceans*, *122*, 4939–4961, doi:10.1002/2016JC012471.

Received 14 OCT 2016
Accepted 21 APR 2017
Accepted article online 27 APR 2017
Published online 17 JUN 2017

Altered inherent optical properties and estimates of the underwater light field during an Arctic under-ice bloom of *Phaeocystis pouchetii*

Alexey K. Pavlov[1], Torbjørn Taskjelle[2], Hanna M. Kauko[1], Børge Hamre[2], Stephen R. Hudson[1], Philipp Assmy[1], Pedro Duarte[1], Mar Fernández-Méndez[1], C. J. Mundy[3], and Mats A. Granskog[1]

[1]Norwegian Polar Institute, Fram Centre, Tromsø, Norway, [2]Department of Physics and Technology, University of Bergen, Bergen, Norway, [3]Centre for Earth Observation Science, University of Manitoba, Winnipeg, Manitoba, Canada

Abstract In spring 2015, we observed an extensive phytoplankton bloom of *Phaeocystis pouchetii*, with chlorophyll *a* concentrations up to 7.5 mg m^{-3}, under compact snow-covered Arctic sea ice at 80–81°N during the Norwegian young sea ICE (N-ICE2015) expedition. We investigated the influence of the under-ice bloom on inherent optical properties (IOPs) of the upper ocean. Absorption and scattering in the upper 20 m of the water column at visible wavebands increased threefold and tenfold, respectively, relative to prebloom conditions. The scattering-to-absorption ratio during the *Phaeocystis* under-ice bloom was higher than in previous Arctic studies investigating diatom blooms. During the bloom, absorption by colored dissolved organic matter (at 375 nm), seemingly of autochthonous origin, doubled. Total absorption by particles (at 440 nm), dominated by phytoplankton (>90%), increased tenfold. Measured absorption and scattering in the water were used as inputs for a 1D coupled atmosphere-ice-ocean radiative transfer model (AccuRT) to investigate effects of altered IOPs on the under-ice light field. Multiple scattering between sea ice and phytoplankton in the ocean led to an increase in scalar irradiance in the photosynthetically active radiation range (E_o(PAR)) at the ice-ocean interface by 6–7% compared to prebloom situation. This increase could have a positive feedback on ice-algal and under-ice phytoplankton productivity. The ratio between E_o(PAR) and downwelling planar irradiance (E_d(PAR)) below sea ice reached 1.85. Therefore, the use of E_d(PAR) might significantly underestimate the amount of PAR available for photosynthesis underneath sea ice. Our findings could help to improve light parameterizations in primary production models.

1. Introduction

Understanding, estimating, and predicting primary productivity in the ice-covered Arctic Ocean has been particularly difficult, despite the extensive research efforts in the past decade [e.g., *Gradinger*, 2009; *Mundy et al.*, 2009; *Lee et al.*, 2010; *Arrigo and van Dijken*, 2015; *Fernández-Méndez et al.*, 2015; *Slagstad et al.*, 2015]. Despite significant advances in the understanding of the topic, even an agreement on the overarching mechanisms (light versus nutrient limitation) controlling under-ice primary production across the entire Arctic Ocean is difficult to achieve, due to large regional differences and variability [e.g., *Popova et al.*, 2012; *Vancoppenolle et al.*, 2013; *Arrigo et al.*, 2015; *Tremblay et al.*, 2015]. The main challenge arises from a lack of in situ observations, especially outside the summer months and in the central Arctic below the ice [*Hill et al.*, 2013]. Estimation of primary production with coupled physical-biological ice-ocean models is challenged by the complexity of the Arctic system, particularly, the large freshwater discharge, complex bathymetry, stratification, and presence of sea-ice cover [*Slagstad et al.*, 2011; *Popova et al.*, 2012; *Vancoppenolle et al.*, 2013; *Babin et al.*, 2015]. Additionally, ocean color remote sensing techniques, which basin-scale primary production estimates rely upon, are not able to sense through the ice pack and the frequent cloud cover in the Arctic summer [*Bélanger et al.*, 2007; *Babin et al.*, 2015].

When it comes to light, the Arctic Ocean is a unique environment as it experiences large seasonality in incoming solar radiation, varying in intensity and day length based on latitude [*Sakshaug and Holm-Hansen*, 1984]. Furthermore, the snow-covered sea ice shades the surface layer from sunlight in spring and summer [*Perovich*, 1996; *Mundy et al.*, 2007; *Nicolaus et al.*, 2013; *Arndt and Nicolaus*, 2014], when levels of incoming

solar radiation are at their maximum and when the main annual pulse of primary production occurs [*Leu et al*., 2015]. Beneath sea ice, propagation of solar radiation is mainly controlled by optical properties of the upper ocean [e.g., *Mobley*, 1994]. Recent studies have highlighted the optical heterogeneity of Arctic waters across different regions, with different constituents dominating light attenuation. Phytoplankton strongly attenuates solar radiation in the visible wavelengths, while detritus attenuates light in both visible and ultraviolet ranges [*Matsuoka et al*., 2007, 2011; *Doxaran et al*., 2012; *Balch et al*., 2014; *Granskog et al*., 2015]. Significant contribution of terrigenous colored dissolved organic matter (CDOM) that strongly attenuates solar radiation in the ultraviolet and visible range in the upper ocean layer has also been highlighted [*Granskog et al*., 2007, 2015; *Hill*, 2008; *Matsuoka et al*., 2012; *Pavlov et al*., 2015, 2016b]. In spring and summer, sea-ice melt also influences the optical properties of the underlying water column, and these effects have shown to be dependent on the age of the ice (multiyear versus first-year) and varying between the Eurasian Basin and Western Arctic [*Bélanger et al*., 2013; *Granskog et al*., 2015; *Logvinova et al*., 2016]. For example, *Bélanger et al*. [2013] found that melting multiyear ice acts as a source of nonalgal particles (detritus) to the upper ocean layer in the Beaufort Sea, while *Granskog et al*. [2015] demonstrated that melting ice (a mix of both first-year and multiyear ice) originating from the Transpolar Drift has relatively low absorption by dissolved matter and particles, and therefore, rather dilute the stronger absorption signal of underlying, CDOM-rich, Polar Water. Furthermore, the spatial heterogeneity of the sea ice surface in advanced stages of melt influences the light field with depth [*Frey et al*., 2011; *Katlein et al*., 2016].

Recent changes in Arctic sea-ice state, observed as a decrease in sea-ice extent, thickness, and volume [*Meier et al*., 2014], have led to a number of studies showing the potential for increased solar flux through the ice cover [*Arndt and Nicolaus*, 2014; *Nicolaus et al*., 2012], potentially resulting in higher primary production by ice algae and phytoplankton [*Meier et al*., 2014; *Arrigo and van Dijken*, 2015; *Fernández-Méndez et al*., 2015]. In this context, the importance of a proper description of the underwater light field for improved estimation of Arctic primary production was emphasized by *Babin et al*. [2015], in their recent review on satellite and model-based estimates of Arctic primary production, who pointed out that "the impact of optical complexity [of Arctic surface waters] is particularly worrying."

Contrary to previous assumptions about negligible under-ice production, recent observations of under-ice blooms below heavily ponded ice in the Western Arctic are contributing to a shift in understanding of primary production in the Arctic Ocean [*Fortier et al*., 2002; *Arrigo et al*., 2012, 2014; *Mundy et al*., 2009, 2014]. Our perception of a clear ocean beneath the ice, virtually void of photosynthetic organisms (phytoplankton), has shifted toward potential biological hotspots beneath the sea ice. Alongside this, our knowledge about optical properties of the ice-covered Arctic Ocean, used to be compared to clearest natural waters [*Apollonio*, 1959; *Smith*, 1973], has also developed. Particularly, the study of *Pegau* [2002] for the first time demonstrated the effects of an under-ice bloom on optical properties of the water column. Recent works of *Balch et al*. [2014] and *Neukermans et al*. [2014, 2016] also helped to better understand the relationships between under-ice blooms and optical properties of the water column. Despite findings of those few studies on optical properties of Arctic under-ice blooms, little is still known about the topic, particularly the various physical and biological implications and feedbacks.

In this study, we investigate the effects of a *Phaeocystis pouchetii* (hereafter *Phaeocystis*) bloom on inherent optical properties (IOPs) of waters underneath a compact sea-ice pack. The bloom was observed in May–June 2015 at 80–81°N in the Eurasian Basin of the Arctic Ocean, during the N-ICE2015 expedition [*Granskog et al*., 2016]. By means of radiative transfer modeling, we further examine how changes in IOPs of the water column during the bloom affect the underwater light field, and discuss the potential biological implications and feedbacks.

2. Materials and Methods

2.1 In Situ Measurements, Sampling, and Data Processing

Observations were carried out during the N-ICE2015 expedition north-west of Svalbard in January–June 2015 with R/V Lance. Four ice camps were established on ice floes that drifted with the ice pack, in the southern Nansen Basin and over the Yermak Plateau [*Granskog et al*., 2016]. Here we focus on observations carried out during drifts of Floe 3 and Floe 4, covering the Arctic spring from 18 April to 22 June (Figure 1).

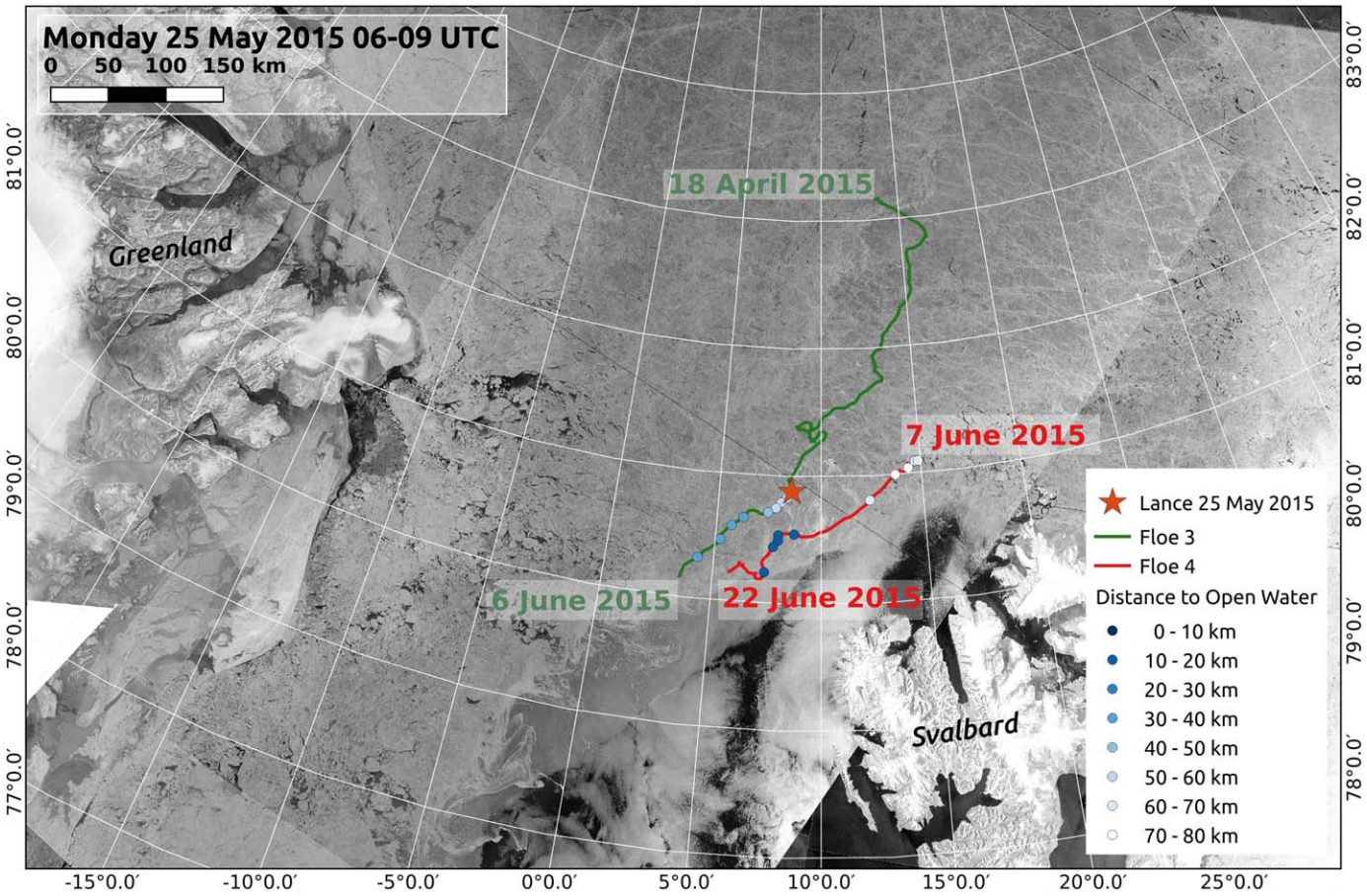

Figure 1. Satellite image of the study area on 25 May with drift tracks for Floes 3 and 4 (start and end dates of drifts indicated). The location of R/V Lance on 25 May is marked with an orange star. Dots on tracks correspond to dates when satellite images were available to estimate a distance between the position of R/V Lance and ice camp to open water (displayed on legend). RADARSAT-2 images provided by NSC/KSAT under the Norwegian-Canadian agreement. RADARSAT-2 Data and Products © MacDonald, Dettwiler, and Associates Ltd (2013) All Rights Reserved. RADARSAT is an official mark of the Canadian Space Agency.

In situ profiles of optical properties were made from a heated tent established on the sea ice several hundred meters away from the ship. Profiles of absorption and attenuation coefficients were measured with two different instruments during the drifts of both Floes 3 and 4 [*Taskjelle et al*., 2016a; *Pavlov et al*., 2016a]. An a-Sphere (HOBI Labs, USA) measured absorption ($a(\lambda)$, excluding absorption by pure water) between 350 and 750 nm at 1 nm resolution, and an ac-9 (WET Labs, Philomath, OR, USA) measured absorption ($a(\lambda)$, excluding absorption by pure water) and beam attenuation ($c(\lambda)$, excluding attenuation by pure water), which is a sum of absorption and scattering at nine distinct wavelengths: 412, 440, 488, 510, 532, 555, 650, 676, and 715 nm (see full list of symbols and units in Table 1). Measurements by a-Sphere were done down to about 100 m, while the majority of ac-9 measurements only covered the upper 20 m of the water column (due to cable length limitations). The a-Sphere was codeployed with a Seabird 911 CTD sensor, calibrated before and after the expedition. The ac-9 was usually deployed independently right after the a-Sphere cast. Data from corresponding CTD profiles were used for temperature and salinity correction of spectral absorption data obtained with ac-9 and a-Sphere following *Röttgers et al*. [2014]. Absorption data from the ac-9 were corrected for scattering effects by subtracting the measured absorption at the wavelength of minimum absorption (usually 715 nm, in some cases 650 nm, where the value at 650 nm was lower than at 715 nm) [*Zaneveld et al*., 1994]. Absorption spectra from a-Sphere were additionally smoothed to reduce the noise (LOESS method) [*Cleveland*, 1979].

Right after or before most optical casts, a micro-rosette (Hydro-Bios Slimline6) was used to collect water samples at discrete depths from the surface down to 100 m for analysis of absorption by CDOM, particle absorption ($a_p(\lambda)$), and chlorophyll *a* (Chl *a*) concentration. These were collected into sample bottles that were transported in an insulated, opaque cooler immediately to the ship for onboard processing.

Table 1. Symbols, Abbreviations and Units Used in this Study (in Alphabetic Order)

Description and (units)	Symbol
Beam attenuation coefficient excluding attenuation by pure water (m^{-1})	$c(\lambda)$
Chlorophyll *a* (mg m^{-3})	Chl *a*
Chl *a* specific algal absorption coefficient (m^2 (mg Chl *a*)$^{-1}$)	$a^*_{\varphi}(\lambda)$
Colored or chromophoric dissolved organic matter	CDOM
CDOM absorption coefficient (m^{-1})	$a_{CDOM}(\lambda)$
Detrital (depigmented) absorption coefficient (m^{-1})	$a_d(\lambda)$
Diffuse attenuation coefficient of E_d in the PAR range (m^{-1})	$K_d(PAR)$
Diffuse attenuation coefficient of E_o in the PAR range (m^{-1})	$K_o(PAR)$
Downwelling planar irradiance: spectral (W m^{-2} nm^{-1}); in the PAR range (W m^{-2})	$E_d(\lambda)$; E_d(PAR)
For biological applications, radiometric units are converted to photometric units of (μmol photons m^{-2} s^{-1})	
Downwelling scalar irradiance: spectral (W m^{-2} nm^{-1}); in the PAR range (W m^{-2})	$E_{od}(\lambda)$; E_{od}(PAR)
Empirical coefficients for power law $a_x(\lambda)=A_x(\lambda)\cdot[Chla]^{B_x(\lambda)}$, where *x* is either *p*, *φ*, *d*, *CDOM* or (none; for total nonwater absorption) (dimensionless)	$A_x(\lambda)$, $B_x(\lambda)$
Optical density (absorbance) of particles on filters (dimensionless)	$OD_s(\lambda)$
Optical density (absorbance) of particles in suspension (dimensionless)	$OD_{sus}(\lambda)$
Photosynthetically active radiation 400–700 nm	PAR
Phytoplankton (algal) absorption coefficient, (m^{-1})	$a_{\varphi}(\lambda)$
Scalar (spherical) irradiance: spectral (W m^{-2} nm^{-1}); in the PAR range (W m^{-2})	$E_o(\lambda)$; E_o(PAR)
Scattering coefficient excluding scattering by pure water (m^{-1})	$b(\lambda)$
Spectral slope of CDOM absorption spectra in the wavelength range λ_1-λ_2, (μm^{-1}); e.g., $S_{300-650}$	$S_{\lambda 1-\lambda 2}$
Spectral slope ratio, $S_{275-295}$: $S_{350-400}$	S_R
Total non-water absorption coefficient (m^{-1})	$a(\lambda)$
Total particle absorption coefficient (m^{-1})	$a_p(\lambda)$
Upwelling planar irradiance: spectral (W m^{-2} nm^{-1}); in the PAR range (W m^{-2})	$E_u(\lambda)$; E_u(PAR)
Upwelling scalar irradiance: spectral (W m^{-2} nm^{-1}); in the PAR range (W m^{-2})	$E_{ou}(\lambda)$; E_{ou}(PAR)
Wavelength (nm)	λ

Chl *a* and $a_p(\lambda)$ samples were filtered through 25 mm Whatman GF/F (GE Healthcare, Little Chalfont, UK) filters under low vacuum pressure (ca. −30 kPa) and shaded from excess light. For details about collection of samples for phytoplankton identification, see *Assmy et al*. [2017]. The $a_p(\lambda)$ samples were stored at −80°C until analysis. CDOM samples were filtered with 0.2 μm membrane syringe filter (PALL Acrodisc, PALL corporation, Ann Arbor, USA) connected to acid-washed all-plastic syringes or through prerinsed 0.2 μm Millipore Opticap XL filter capsules (Merck Millipore, Billerica, MA, USA) into precombusted amber glass vials. Samples were stored at 4°C in dark until analysis.

2.2. Analytical Methods

Chl *a* was extracted with 100% methanol at 5°C for 24 h following *Holm-Hansen and Riemann* [1978] and then measured using a Turner 10-AU Fluorometer (Turner Designs, San Jose, USA). The identification of species was performed by an expert taxonomist (Jozef Wiktor) at the Institute of Oceanology Polish Academy of Sciences (IOPAS) using light microscopy methods. Furthermore, HPLC pigment analysis also confirmed *Phaeocystis* dominance [see *Assmy et al*., 2017 for details].

CDOM absorbance was measured with a Shimadzu UV-2401PC spectrophotometer (Shimadzu Corporation, Kyoto, Japan) between 240 and 700 nm with 0.5 nm resolution. Quartz cells of 10 cm with fresh ultrapure water were used as reference. Absorbance values were baseline corrected by fitting with the equation following *Stedmon et al*. [2000], which has a constant that allows accounting for minor shifts at longer wavelengths. Absorption coefficients a_{CDOM} (m^{-1}) were then calculated following:

$$a_{CDOM}(\lambda)=\ln(10)\cdot\frac{A(\lambda)}{l} \quad (1)$$

where $A(\lambda)$ is the absorbance at a given wavelength λ and *l* is the path length of the cuvette in meters.

CDOM absorption spectral slopes were estimated with a nonlinear exponential fit [*Stedmon and Markager*, 2001] for different wavelength ranges, including 300–650 nm, $S_{300-650}$, 350–400 nm, $S_{350-400}$, and 275–295 nm, $S_{275-295}$. Spectral slope ratio, S_R, was calculated after *Helms et al*. [2008] as $S_{275-295}$: $S_{350-400}$. Data on CDOM absorption are available in *Pavlov et al*. [2017].

Particle absorbance was measured with a Shimadzu UV-2450 dual-beam spectrophotometer with an integrating sphere (ISR-2200, Shimadzu Corporation, Kyoto, Japan) between 240 and 800 nm, following the

modified method described in *Tassan and Ferrari* [2002], and recommendations in *Tilstone et al*. [2002] and *Mueller et al*. [2003]. The procedure is described in more detail in *Kauko et al.* [2017b]. Blank filters prepared with ultrapure water in the field throughout the expedition were used as a wet reference to account for light scattering and absorption by the filter. Bleaching was done with 400 μL of sodium hypochlorite (NaClO with 1% active chlorine) for 10 min, and rinsing with 30 mL of artificial seawater (60 g Na_2SO_4 in 1 L of ultrapure water). Absorbance (optical density) of particles on filters ($OD_s(\lambda)$) was converted to optical density of particles in suspension ($OD_{sus}(\lambda)$) following *Tassan and Ferrari* [2002; equation (10)].

$$OD_{sus}(\lambda) = 0.423 \cdot OD_s(\lambda) + 0.479 \cdot OD_s(\lambda)^2 \quad (2)$$

$OD_{sus}(\lambda)$ was then converted to a total particle absorption coefficient $a_p(\lambda)$:

$$a_p(\lambda) = \ln(10) \cdot \frac{OD_{sus}(\lambda)}{l} \quad (3)$$

where l is the hypothetical path length in meters, based on the ratio between the filtered sample volume and sample area diameter on the filter. A baseline correction was done relative to the mean absorption values at 750–800 nm.

Total particle absorption ($a_p(\lambda)$, m^{-1}) can be further divided into detrital (depigmented particles) absorption ($a_d(\lambda)$, m^{-1}; measured spectra after bleaching). Subtracting detrital from total absorption gives the phytoplankton (algal) absorption ($a_\varphi(\lambda)$, m^{-1}). Chl *a*-specific phytoplankton absorption ($a^*_\varphi(\lambda)$, m^2 (mg Chl *a*)$^{-1}$) is obtained by dividing $a_\varphi(\lambda)$ by the corresponding Chl *a* values (in mg m^{-3}). Data on particle absorption are available in *Kauko et al*. [2017a].

Relationships between Chl *a* and all absorbing constituents were fitted with power law functions (equation (4)) following *Bricaud et al*. [1998], where [Chl *a*] is a concentration of Chl *a* and *x* represents each of the absorbing constituents: phytoplankton, detritus, total particles, CDOM, and total nonwater absorption.

$$a_x(\lambda) = A_x \cdot [Chl\ a]^{B_x(\lambda)} \quad (4)$$

2.3. AccuRT Radiative Transfer Modeling

The AccuRT radiative transfer model (Geminor Inc., Maplewood, NJ, USA) was used to simulate the light field beneath the ice. AccuRT, formerly called c-disort, [e.g., *Hamre et al*., 2004; *Taskjelle et al*., 2016b; *Thomas and Stamnes*, 2002] is a plane parallel coupled atmosphere-snow-ice-ocean radiative transfer model that uses the discrete ordinates method to solve the radiative transfer equation. It has been previously validated for different types of Arctic sea ice and open water conditions [*Gjerstad et al*., 2003; *Hamre et al*., 2004; *Taskjelle et al*., 2016b,2017a]. IOPs of snow and ice are determined by specifying the size and volume fractions of spherical inclusions, and using a parameterization based on Mie calculations [*Stamnes et al*., 2011]. Absorption of pure ice [*Warren and Brandt*, 2008] and pure water [*Pope and Fry*, 1997; *Segelstein*, 1981] is obtained from literature. Average absorption and scattering ($b(\lambda) = c(\lambda) - a(\lambda)$) coefficients in top 20 m from ac-9 data were added to the water column, and the Henyey-Greenstein phase function was applied with an asymmetry parameter g = 0.92, which is close to the 0.924 that gives the best fit to the Petzold average particle phase function [e.g., *Mobley*, 1994]. Irradiances were calculated with a spectral resolution of 1 nm. The vertical resolution was 10 cm from the surface down to 15 m depth, and 1 m from 15 to 40 m. More details about description of the model setup are given in *Taskjelle et al*. [2017a]. The solar zenith angle was set to 60°, which is representative of midday values for the position of the ice camp on 26 May 2015 at about 80.8°N. A thin cloud layer is considered, representative of the persistent clouds encountered in the region in May and June [*Cohen et al.*, 2017]. For all model simulations, the same incident solar spectrum on top of the atmosphere was used.

Three cases of different surface conditions were considered [*Taskjelle et al*., 2017a; *Assmy et al*., 2017], representing the primary surface conditions during the expedition:

1. 130 cm thick ice with 40 cm of snow, representative of large areas of thick ice in the region;
2. 20 cm thick ice with 2 cm of snow, representative of the refrozen lead in the study area;
3. open water, encountered toward the end of the expedition and in leads.

Four settings were considered regarding the IOPs of the water column (Table 2):

Table 2. Total Water Absorption (a) and Attenuation (c; Sum of Absorption and Scattering) Used in AccuRT Simulations[a]

	Prebloom		Bloom		Pegau Turbid		Coastal	
Wavelength	a (m^{-1})	c (m^{-1})	a (m^{-1})	c (m^{-1})	a (m^{-1})	c (m^{-1})	a (m^{-1})	c (m^{-1})
350	0.118	0.161	0.273	0.657	0.233	0.406	1.280	3.789
412	0.061	0.107	0.182	0.596	0.144	0.308	0.905	3.311
440	0.049	0.089	0.177	0.572	0.109	0.270	0.706	3.011
488	0.026	0.086	0.123	0.561	0.075	0.233	0.465	2.718
510	0.044	0.100	0.110	0.579	0.075	0.233	0.382	2.635
532	0.052	0.111	0.102	0.591	0.072	0.227	0.344	2.547
555	0.064	0.126	0.094	0.610	0.077	0.228	0.300	2.461
650	0.340	0.397	0.359	0.865	0.340	0.471	0.440	2.541
676	0.457	0.510	0.517	0.967	0.485	0.608	0.553	2.554
715	1.008	1.049	1.007	1.510	1.007	1.130	1.007	3.008

[a]For prebloom and bloom conditions, values are averages for the upper 20 m over the periods defined in the text. A "Pegau turbid" case from *Pegau* [2002] and an example from Norwegian coastal waters [*Hamre et al*., 2003] are included for comparison. Absorption by pure water [*Pope and Fry*, 1997; *Sogandares and Fry*, 1997] and scattering from the clearest natural waters [*Smith and Baker*, 1981] are added to the values measured by ac-9 instrument to obtain total absorption and attenuation. Values at 350 nm are extrapolated linearly from measurements at 412, 440, 488, and 510 nm following *Granskog et al*. [2015].

1. Prebloom conditions, with absorption and beam attenuation values averaged over the upper 20 m from the period 24 April 24 to 14 May. Typical Chl *a* concentrations before the bloom were below 1 mg m^{-3};
2. Bloom conditions, with absorption and attenuation values averaged over the upper 20 m from the period 26–30 May. Typical Chl *a* concentrations during the bloom were between 1 and 7.5 mg m^{-3};
3. Under-ice bloom encountered by *Pegau* [2002] (termed the "*Pegau* turbid" case) dominated by phytoflagellates and diatoms [*Sherr et al*., 2003]. Typical Chl *a* concentrations during the bloom were in the range of 0.5–0.9 mg m^{-3};
4. Coastal bloom in the Norwegian Sea dominated by *Emiliania huxleyi* as an example of higher scattering and absorption in the water column [*Hamre et al*., 2003]. Typical Chl *a* concentrations during the bloom were in the range of 1–3 mg m^{-3}.

Key output from AccuRT includes surface-incident, in-ice and in-water profiles of spectral downwelling and upwelling scalar irradiance ($E_{od}(\lambda)$ and $E_{ou}(\lambda)$), and spectral downwelling and upwelling planar (cosine) irradiance ($E_d(\lambda)$ and $E_u(\lambda)$), at specified wavelengths in ultraviolet, visible, and near-infrared ranges. Scalar (spherical) irradiance ($E_o(\lambda)$) was calculated as a sum of $E_{od}(\lambda)$ and $E_{ou}(\lambda)$. For biological applications, spectral irradiances were converted from W m^{-2} nm^{-1} to μmol photons m^{-2} s^{-1} [e.g., *Mobley*, 1994]. Based on spectral values, scalar and planar irradiances in the PAR waveband were calculated by integrating the spectral irradiances from 400 to 700 nm.

3. Results and Discussion

3.1. Changes in Inherent Optical Properties (IOP) of the Water Column Caused by the Phytoplankton Bloom

3.1.1. Evolution of the Bloom and IOP in Relation to Hydrographic Changes and Sea-Ice Conditions

The study area north-west of Svalbard archipelago is generally influenced by the inflow of warm and saline Atlantic Water (AW) advected northward by the West Spitsbergen Current [e.g., *Rudels et al*., 2015]. The vertical structure of water masses in the top 100 m encountered during the campaign typically included Polar Surface Water (PSW), underlain by Modified Atlantic Water (MAW) or AW [*Meyer et al*., 2017].

The ice camps generally drifted in a south-west direction toward the Fram Strait, which is a common drift pattern as a part of the Transpolar Drift system [e.g., *Kwok*, 2009]. An extensive under-ice phytoplankton bloom (Figure 2) was encountered over the Yermak Plateau on 25 May 2015, when the ice camp was approximately 80 km away from the open ocean (Figure 3a). The occurrence of the bloom coincided with the thinning of the mixed PSW layer and shoaling of the underlying AW/MAW, which was still deeper than 100 m at the time when the bloom was initially observed [*Assmy et al*., 2017]. Starting from mid-June AW was frequently present below 50 m [*Meyer et al*., 2017]. Here we define "bloom" as a period when relatively high Chl *a* concentrations above 1 mg m^{-3} in the top 40–50 m were observed (from 25 May onward). The area around the ice camp was covered by compact sea ice with thick snow cover. However, leads with open water or thinner ice covered 1–33% of the study area from late May to late June, which through increased

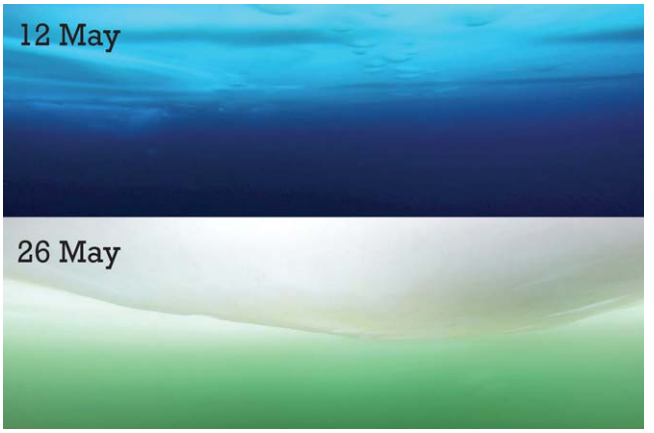

Figure 2. Under-ice photo taken before (12 May 2015) and during (26 May 2015) the under-ice phytoplankton bloom. Copyright: C.J. Mundy, University of Manitoba.

light transmission made it possible for the bloom to develop under the ice [*Assmy et al.*, 2017; *Taskjelle et al.*, 2017a]. As identified by light microscopy and high performance liquid chromatography (HPLC) techniques, the under-ice bloom was dominated by *Phaeocystis pouchetii* accounting for 55–92% of phytoplankton abundance with maximum Chl *a* values of up to 7.5 mg m^{-3} [*Assmy et al.*, 2017, Figure 2]. The other species present, such as some pelagic diatoms, did not contribute substantially to the total biomass in most of the stations [*Assmy et al.*, 2017]. Vertical distribution of biomass (as indicated by Chl *a*) was generally relatively uniform from the surface down to 30–40 m during Floe 3 drift, and more variable during Floe 4 (Figure 3b). Toward the end of both drifts (Floe 3 and 4), when the ice camp was closer than 30 and 15 km to open water, respectively, the biomass generally decreased in the upper 10–15 m. These changes in the vertical distribution of Chl *a* were coincident with a depletion in nitrate inventory in upper 50 m [*Assmy et al.*, 2017] and with increased stratification. The increase in stratification was caused by freshening of the surface layer due to increased sea-ice melt as indicated by observations of bottom sea-ice melt [*Provost et al.*, 2017], and due to an increase in density of the underlying layer of AW, as well as its shoaling [*Meyer et al.*, 2017; *Assmy et al.*, 2017].

This bloom was unusual because it developed under a 1–2 m thick ice pack covered by thick snow early in spring, before surface melt had commenced and melt ponds had formed [*Assmy et al.*, 2017]. In contrast, more typical blooms would be the ones developing in the marginal ice zone or in open water, and are often dominated by diatoms [e.g., *Von Quillfeldt*, 2000; *Barber et al.*, 2015]. This bloom was possible due to increased light transmission through open and refrozen leads in the area [*Assmy et al.*, 2017], which highlights the potential for phytoplankton blooms early in the season when nutrients are relatively abundant in the under-ice water column but light is usually a limiting factor [*Mundy et al.*, 2009; *Tremblay and Gagnon*, 2009].

The transition from prebloom to bloom conditions affected IOPs of the water column, which can be used to retrieve information about the bloom itself. The most detailed temporal and vertical coverage of IOPs during the campaign was obtained with a-Sphere casts (Figure 3c). Total absorption by dissolved and particulate matter at 440 nm ($a(440)$, excluding pure water absorption), corresponding to the primary phytoplankton absorption peak, clearly demonstrates both the temporal evolution of the bloom and its vertical extent down to 40–50 m and 25–30 m during Floe 3 and Floe 4 drifts, respectively (Figure 3c). The majority of biomass was confined to PSW during our observations. Therefore, differences at the end of Floes 3 and 4 are likely to be explained by the thinning of the PSW layer, which did not exceed 30–40 m at the end of the Floe 4 compared to 50–60 m at the end of the Floe 3 drift [*Meyer et al.*, 2017]. While elevated $a(440)$ values were observed from 25 May onward, some day-to-day variability can also be observed (Figure 3c), potentially pointing at a spatiotemporal patchiness of biomass distribution. The average vertical profiles of $a(440)$ and Chl *a* during the bloom (inset in Figure 3c) are consistent, and show higher values at the surface, with a subsurface peak around 25 m, followed by a more rapid decrease with depth during the bloom, which is likely to reflect the vertical structure of the water column.

The evolution of depth averaged (upper 20 m) absorption and scattering spectra obtained by the ac-9 instrument is shown in Figure 4. The rapid transition to bloom conditions is reflected in the drastic increase in both spectral absorption and scattering. The shapes of scattering and absorption spectra are inversely related, which is often observed in oceanic waters when phytoplankton dominates the total absorption and scattering [e.g., *Babin et al.*, 2003]. Before the bloom, $a(\lambda)$ was below 0.1 m^{-1} with slightly higher values toward shorter wavelengths, reflecting absorption by both particles and CDOM. Values of $b(\lambda)$ were also below 0.1 m^{-1}, and were generally spectrally uniform. The average ratio between $b(\lambda)$ and $a(\lambda)$ was below 2.

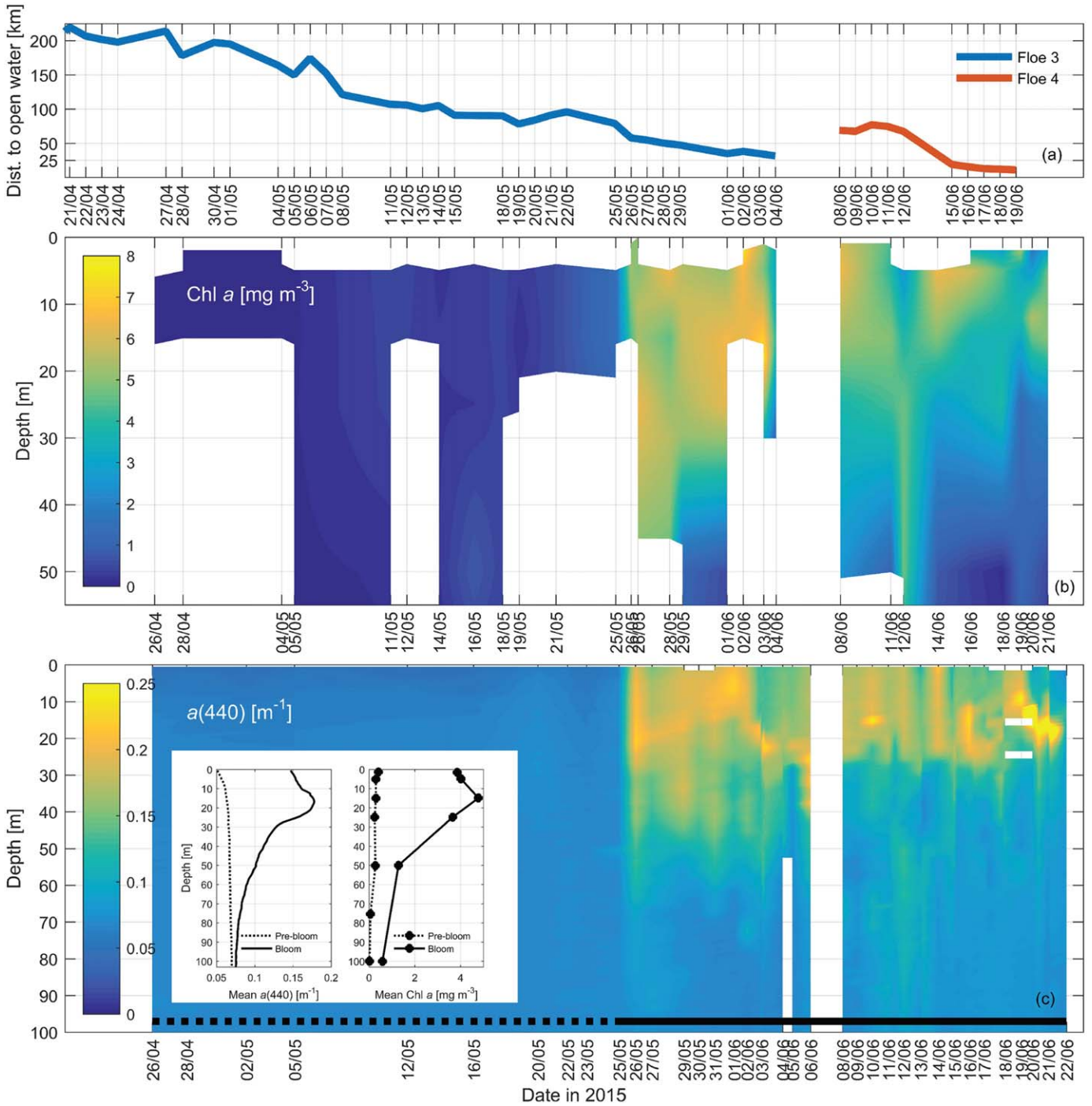

Figure 3. (a) Distance from the ice camp to open water during the drifts of Floes 3 and 4; (b) Evolution of Chl *a* concentration from the surface to 50 m; (c) Evolution of the absorption coefficient by dissolved and particulate matter at 440 nm (*a*(440)) from the surface to 100 m measured by the a-Sphere instrument. Dates indicate days when profiles were taken. The inset in Figure 3c shows average vertical profiles of *a*(440) and Chl *a* before the bloom (prior to 25 May) and for the bloom period (after 25 May). Periods of prebloom and bloom conditions are indicated by the dashed and solid lines at the bottom of the section plot (Figure 3c).

These values are comparable to Atlantic Waters of the West Spitsbergen Current in summer [*Granskog et al.*, 2015] and to under-ice measurements prior to the spring bloom in the Canada Basin [*Pegau*, 2002]. The most interesting feature during the bloom was the approximately tenfold increase in scattering, while average absorption only increased by a factor of 2–3, depending on wavelength. This is also confirmed by visual observations of the water under the ice that became more opaque during the bloom (Figure 2). Average

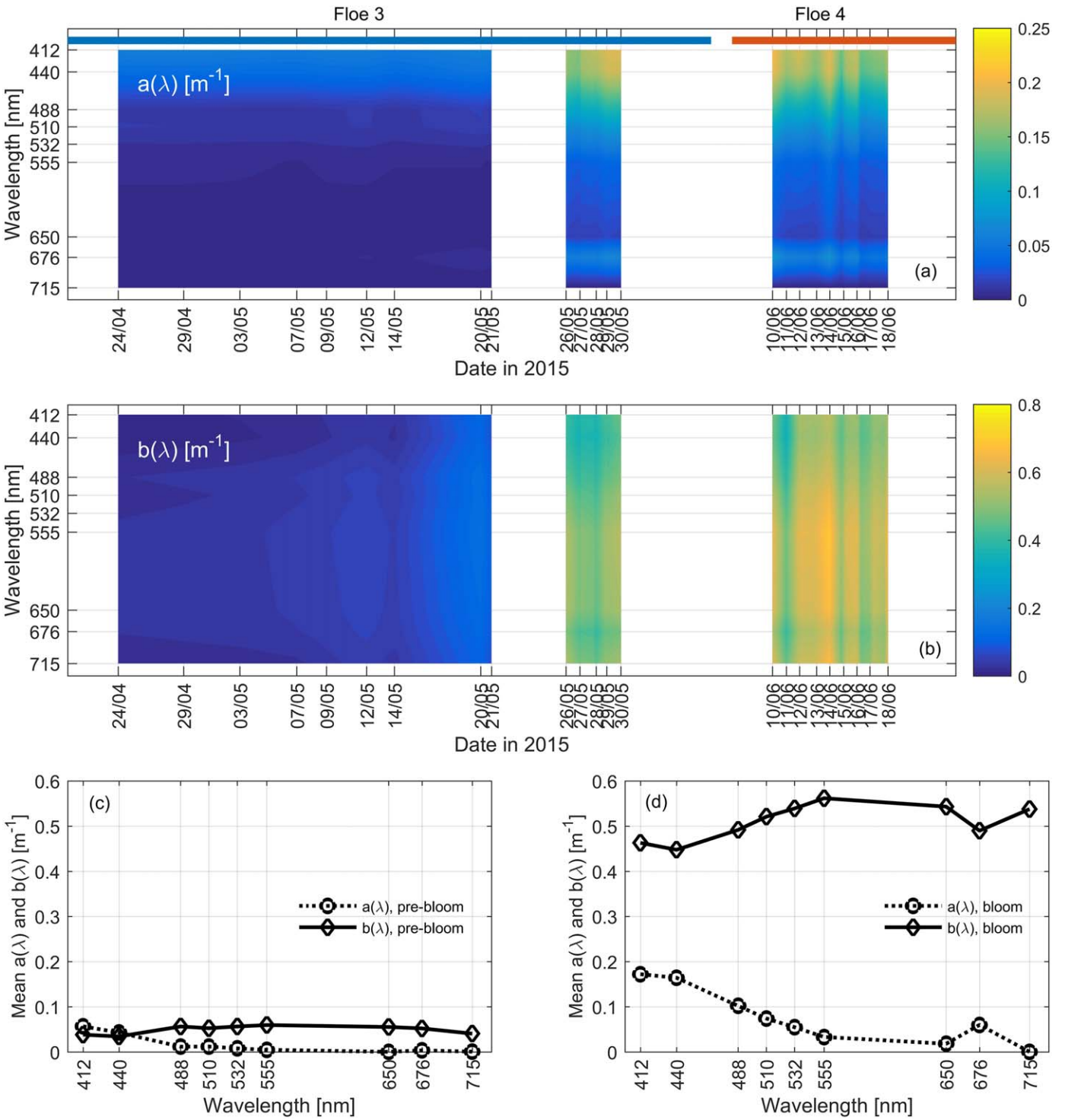

Figure 4. Evolution of (a) spectral absorption coefficient and (b) scattering coefficient averaged over the upper 20 m as obtained from ac-9 casts, between 24 April and 18 June 2015. Dates indicate days when ac-9 casts were taken. (c) and (d) Mean absorption and scattering coefficients before the bloom (prior to 21 May) and during the bloom (26–30 May and 10–18 June), respectively. Floe 3 and 4 drifts are indicated by blue and red lines in (a), while periods of prebloom and bloom conditions are indicated by black dotted and solid lines in Figure 4b.

$b(\lambda)$ was more than 0.5 m^{-1}, and the highest $a(\lambda)$ was observed at shorter wavelengths and at 676 nm (secondary Chl *a* absorption peak), indicating a contribution from CDOM and phytoplankton absorption. Thus, the $b(\lambda)$ to $a(\lambda)$ ratio increased to <3 at 412 and 440 nm, to >10 at longer wavelengths ($>$ 555 nm). During a massive under-ice bloom in the Chukchi Sea dominated by diatoms, *Balch et al.* [2014] reported values of

b(531) of up to 2 m^{-1} and a_p(440) (which does not account for CDOM absorption) of up to 1 m^{-1}. Taking into account spectral dependencies of both absorption and scattering, the ratio between scattering and absorption would be several times lower across the visible wavelengths compared to our study. Therefore, high scattering to absorption ratio is apparently characteristic of *Phaeocystis* blooms. However, we were unable to find previous studies looking specifically at scattering properties of *Phaeocystis* blooms. It has been shown that intact *Phaeocystis* colonies are covered with a thin yet tough and strong skin underlain by a gelatinous layer, and its optical properties are difficult to assess, largely due to the transparency and thinness of this skin [*Hamm et al*., 1999].

3.1.2. Optically Active Substances: Colored Dissolved Organic Matter and Particles

Prior to the bloom (before 25 May), we typically observed relatively uniform CDOM absorption with depth, from surface to 100 m (Figure 5a). A noticeable increase in CDOM absorption occurred in the top 25 m in the beginning of June, and continued toward the end of the Floe 4 (end-June) drift, with an exception of the last sampling station. At the same time, a_{CDOM}(375) at 100 m was relatively low and did not change. Before the bloom, average values of a_{CDOM}(375) were 0.09 $\pm$ 0.03 m^{-1} in top 50 m (Table 3). These values are relatively low and in the same range as those observed in Atlantic waters in the West Spitsbergen Current in late summer and autumn (<0.10 m^{-1}) [*Granskog et al*., 2015; *Pavlov et al*., 2015]. During the bloom, average a_{CDOM}(375) and a_{CDOM}(350) were 0.14 $\pm$ 0.05 and 0.19 $\pm$ 0.06 m^{-1} (Table 3). *Hancke et al*. [2014] reported a_{CDOM}(350) of 0.14–0.17 m^{-1} for both Arctic and Atlantic waters across the Polar front in the ice-free Barents Sea during a spring phytoplankton bloom. Average a_{CDOM}(375) in Atlantic waters of the Greenland Sea in June was 0.15 $\pm$ 0.05 m^{-1} [*Stedmon and Markager*, 2001]. Our values of a_{CDOM} (375) differ from those reported by *Lund-Hansen et al*. [2015] in the Central Arctic Ocean, who observed average a_{CDOM}(375) of 0.52 $\pm$ 0.24 m^{-1} under the ice. Higher CDOM absorption values in their study could be explained by the higher contribution of terrestrial DOM, presumably originating from Siberian rivers, rather than locally produced marine (autochtonous) CDOM [*Granskog et al*., 2012; *Lund-Hansen et al*. 2015]. Relatively low CDOM absorption in our study can likely be explained by differences in mechanisms of PSW formation in our area of study compared to further east and in the central Arctic Ocean. According to *Rudels* [1989], PSW can be formed from two parent water masses: AW and freshwater from riverine run-off, sea-ice melt, and precipitation. The first mechanism would include the entrainment and transformation of cooled AW into the surface layer during sea-ice formation and winter convection. The second mechanism would imply a stronger contribution of riverine runoff in formation of PSW. The first mechanism seems to be the most relevant for our area of study off the continental shelf and not largely affected by riverine runoff rich in terrigenous CDOM. Therefore, CDOM absorption observed in PSW is relatively low in our study compared to e.g., *Lund-Hansen et al*. [2015] and *Granskog et al*. [2012], where the contribution of CDOM-rich halocline waters to formation of PSW is likely to be more significant. Spectral slopes of CDOM absorption spectra in the range 300–650 nm, $S_{300–650}$, were 23.03 $\pm$ 3.51 μm^{-1} and 18.45 $\pm$ 3. μm^{-1}, before and during the bloom, respectively. Decrease in $S_{300–650}$ values indicates a change to a stronger dominance of autochthonous CDOM throughout the campaign. *Stedmon and Markager* [2001] reported $S_{300–650}$ values of 16.9 $\pm$ 3.3 μm^{-1} for AW in the Greenland Sea in summer. *Hancke et al*. [2014] reported slopes for a slightly different wavelength range (350-550 nm), $S_{350–550}$, of 15 $\pm$ 3 and 14 $\pm$ 2 μm^{-1} for Atlantic and Arctic waters during a spring bloom in the Barents Sea.

Noticeable increase in CDOM absorption started approximately 1 week after the bloom onset (Figure 5a), which resulted in the absence of strong relationship between Chl *a* and a_{CDOM}(440) (Figure 8). Such observation is in line with findings by *Kieber et al*. [2009], who did not observe an initial increase in CDOM absorption even with a 100 times increase in Chl *a* concentration during a *Phaeocystis* bloom in the Southern Ocean. Weak correlation between Chl *a* and absorption by CDOM has also been previously reported in the Arctic Ocean [*Cota et al*., 2003; *Wang et al*., 2005; *Matsuoka et al*., 2007; *Pavlov et al*., 2014]. The likely explanation is that CDOM pool in the water column accumulates over time and is controlled by combined biological, chemical and physical effects, not necessarily related to phytoplankton dynamics alone [*Nelson et al*., 1998; *Wang et al*., 2005].

Optical properties of CDOM observed in our study indicate that it is of autochtonous origin, produced during the bloom, with little or no influence from the terrestrial (allochtonous) CDOM. These optical properties include the relatively low a_{CDOM}(375) values (Figure 5a), slope ratio (S_R, Figure 5c) above 1 [*Helms et al*., 2008], and a_{CDOM}(375) versus $S_{300–650}$ relationship (Figure 5d) typical for autochtonous CDOM [cf., *Stedmon and Markager*, 2001]. Similar a_{CDOM}(375) versus $S_{300–650}$ relationships have been previously observed in

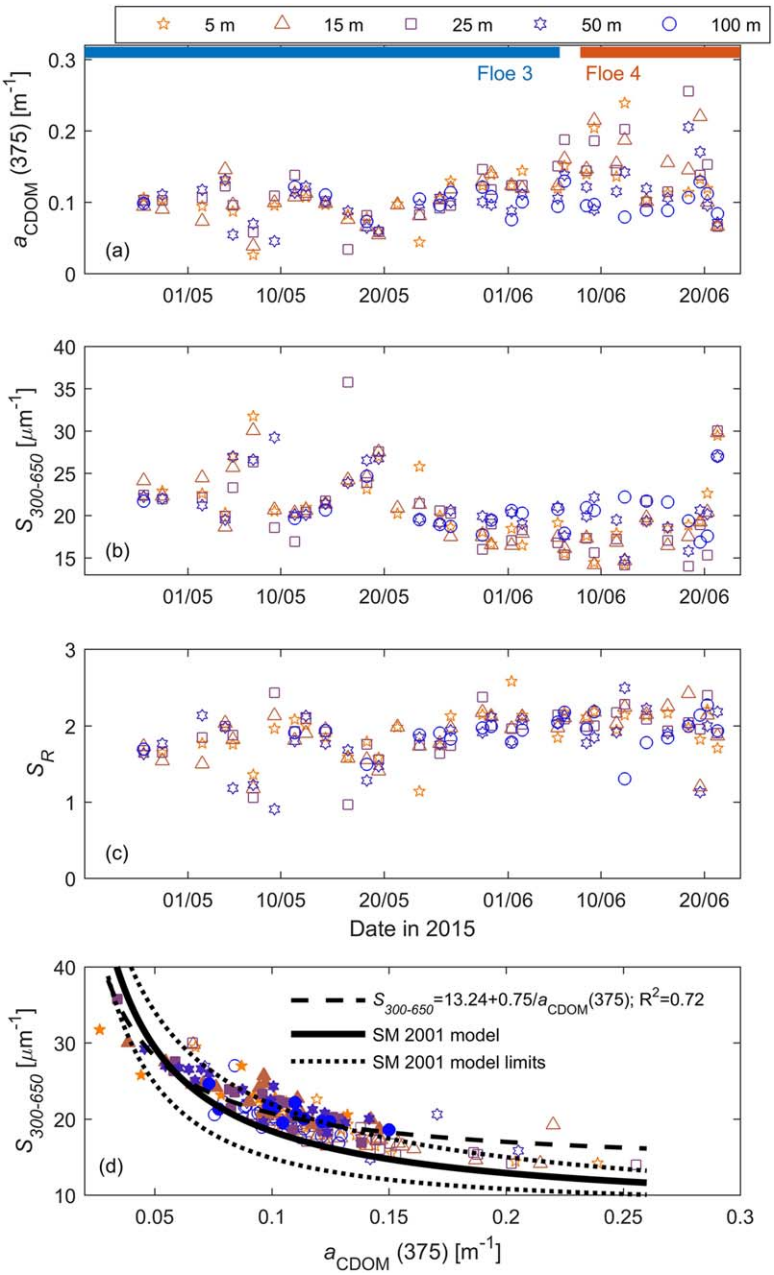

Figure 5. (a) Evolution of absorption coefficient by CDOM at 375 nm ($a_{CDOM}(375)$); (b) CDOM absorption spectral slope for the range 300–650 nm ($S_{300-650}$), and (c) spectral slope ratio (S_R) at discrete sampling depths; (d) $S_{300-650}$ versus $a_{CDOM}(375)$ plot for all samples. Symbols show the same depths as on Figures 5a, 5b, and 5c. A model of *Stedmon and Markager* [2001] for marine CDOM and best fit with similar equation type are also shown. Filled symbols on Figure 5d show data before the bloom onset.

Atlantic-dominated waters [*Pavlov et al*., 2014; *Hancke et al*., 2014], contrary to a number of studies in regions influenced by terrestrial CDOM with weak or no dependence between spectral slope and CDOM absorption values [e.g., *Granskog et al*., 2007].

Total absorption by particles ($a_p(440)$, measured by the filter pad technique) was generally low prior to the bloom onset, and increased tenfold in the Chl *a* maximum layer (20–25 m) during the bloom compared to prebloom conditions (Figure 6a). Absolute values of $a_p(440)$ were below 0.01 m^{-1} in late April, then below 0.02 m^{-1} in May prior bloom onset, and reached up to 0.09–0.11 m^{-1} during the bloom toward the end of drifts on Floes 3 and 4. Total absorption was dominated by phytoplankton, $a_{\varphi}(440)$, as seen from similarity of Figures 6a and 6c, which increased drastically during the bloom. In contrast, absorption by detritus

Table 3. Selected Characteristics of Optically Active Substances (Mean ± Standard Deviation) for Upper 50 m Before (Prior 25 May) and During the Bloom (After 25 May)

	Prebloom					Bloom				
Wavelength (nm)	$a_{CDOM}(\lambda)$ (m^{-1})	$a_p(\lambda)$ (m^{-1})	$a_d(\lambda)$ (m^{-1})	$a_\varphi(\lambda)$ (m^{-1})	$a^*_\varphi(\lambda)$ (m^2 (mg Chl a)$^{-1}$)	$a_{CDOM}(\lambda)$ (m^{-1})	$a_p(\lambda)$ (m^{-1})	$a_d(\lambda)$ (m^{-1})	$a_\varphi(\lambda)$ (m^{-1})	$a^*_\varphi(\lambda)$ (m^2 (mg Chl a)$^{-1}$)
254	1.472 ± 0.104					1.520 ± 0.196				
350	0.137 ± 0.030					0.189 ± 0.058				
375	0.092 ± 0.027					0.135 ± 0.046				
440	0.032 ± 0.018	0.007 ± 0.004	0.001 ± 0.001	0.006 ± 0.004	0.032 ± 0.018	0.064 ± 0.028	0.060 ± 0.029	0.002 ± 0.003	0.058 ± 0.029	0.017 ± 0.005
676		0.003 ± 0.002	0.000 ± 0.000	0.003 ± 0.002	0.024 ± 0.064		0.029 ± 0.014	0.000 ± 0.001	0.029 ± 0.015	0.008 ± 0.002
	$S_{275–295}$ (μm^{-1})	$S_{300–650}$ (μm^{-1})	$S_{350–400}$ (μm^{-1})	S_R		$S_{275–295}$ (μm^{-1})	$S_{300–650}$ (μm^{-1})	$S_{350–400}$ (μm^{-1})	S_R	
	31.18 ± 1.72	23.03 ± 3.51	19.04 ± 5.21	1.73 ± 0.31		28.92 ± 3.15	18.45 ± 3.33	14.35 ± 2.40	2.04 ± 0.26	

(a_d(440)) was low in top 100 m during the whole campaign (Figure 6b), with a_d(440) values below 0.01 m^{-1}, contributing <10% to a_p(440) at the peak of the bloom. When looking at a ternary diagram (Figure 7) showing contributions of three components to the total absorption budget, despite generally low absorption in comparison with other Arctic locations [e.g., *Granskog et al*., 2012; *Matsuoka et al*., 2014] CDOM dominated (60–95%), the nonwater absorption prior to the bloom, which is explained by even lower absorption by other constituents, phytoplankton and detritus. Even during the bloom, at depths below 25 m CDOM was the major contributor to total absorption. Contribution from detritus did not exceed 10% neither prior, nor during the bloom. Contribution of phytoplankton was variable before and during the bloom. During the bloom in top 25 m, it typically contributed 40–65% to the total nonwater absorption.

Information about particle absorption in the study area north-west of Svalbard is limited. For the reference, total particle absorption was previously reported for the Fram Strait waters (78°N) in September by *Pavlov et al*. [2015], who found maximum a_p(440) of up to 0.09–0.10 m^{-1} in surface waters, which is comparable to the present study. At the same time, AW had a_p(440) of 0.047 ± 0.012 and 0.016 ± 0.014 m^{-1} in two consecutive years. During a massive under-ice diatom bloom in the Chukchi Sea (with Chl *a* concentrations exceeding 20 mg m^{-3}), a_p(440) reached up to 1 m^{-1} according to *Balch et al*. [2014], which is one order of magnitude higher compared to our study. In general, based on comparison of typical particle absorption and Chl *a* values in both studies, one could see that Chl *a* specific particle absorption is lower in our case compared to *Balch et al*. [2014], thus, indicating higher pigment packaging and low light acclimation. This is further discussed based on a^*_ϕ(676) values.

Average values of a^*_ϕ(676) in the top 50 m (Table 3, Figure 6d) were 0.023 ± 0.061 and 0.008 ± 0.003 m^2 (mg Chl *a*)$^{-1}$, before and during the bloom, respectively. Larger variability of a^*_ϕ(676) before the bloom might be caused by both low phytoplankton absorption and relatively low Chl *a* values. Average values of a^*_ϕ(676) during the bloom are slightly higher compared to a value of 0.006 m^2 (mg Chl *a*)$^{-1}$, reported for an under-ice bloom in the Chukchi Sea [*Neukermans et al*., 2014], and slightly higher compared to a^*_ϕ(676) of 0.010 ± 0.003 m^2 (mg Chl *a*)$^{-1}$, reported by *Cota et al*. [2003] for a diatom bloom in open waters of the Labrador Sea. *Moisan and Mitchell* [1999] observed similar a^*_ϕ(676) for *Phaeocystis antarctica* under low light experiments. Generally, the low values of a^*_ϕ(676) that we observed during the bloom would indicate that pigments are highly packaged and that phytoplankton was low-light acclimated [e.g., *Johnsen et al*., 1994]. This is in line with findings from *Assmy et al*. [2017], who reported low particulate organic carbon to Chl *a* ratio in the upper 25 m during the bloom, which suggests a relatively high investment in photosynthetic pigments, indicative of shade-acclimation of phytoplankton [*Falkowski*, 1980].

Figure 8 shows bio-optical relationships between Chl *a* and phytoplankton absorption, and Chl *a* and total particle absorption, highlighting prebloom and bloom conditions. Power law functions (equation (4)) are commonly applied to fit this empirical relationships [e.g., *Bricaud et al*., 1998]. Corresponding statistics are presented in Table 4, also including relationships between Chl *a* and absorption by detritus, CDOM and total nonwater absorption.

Generally, we found strong relationships between Chl *a* and a_p(440), and Chl *a* and a_φ(440) based on data from the whole study (R^2 = 0.93 and 0.93, respectively) and during the bloom only (R^2 = 0.86 and 0.87, respectively).The correlation between Chl *a* and a_{CDOM}(440), and Chl *a* and a_d(440) were very low, which has been found in previous Arctic studies [*Cota et al*., 2003; *Wang et al*., 2005; *Matsuoka et al*., 2007].

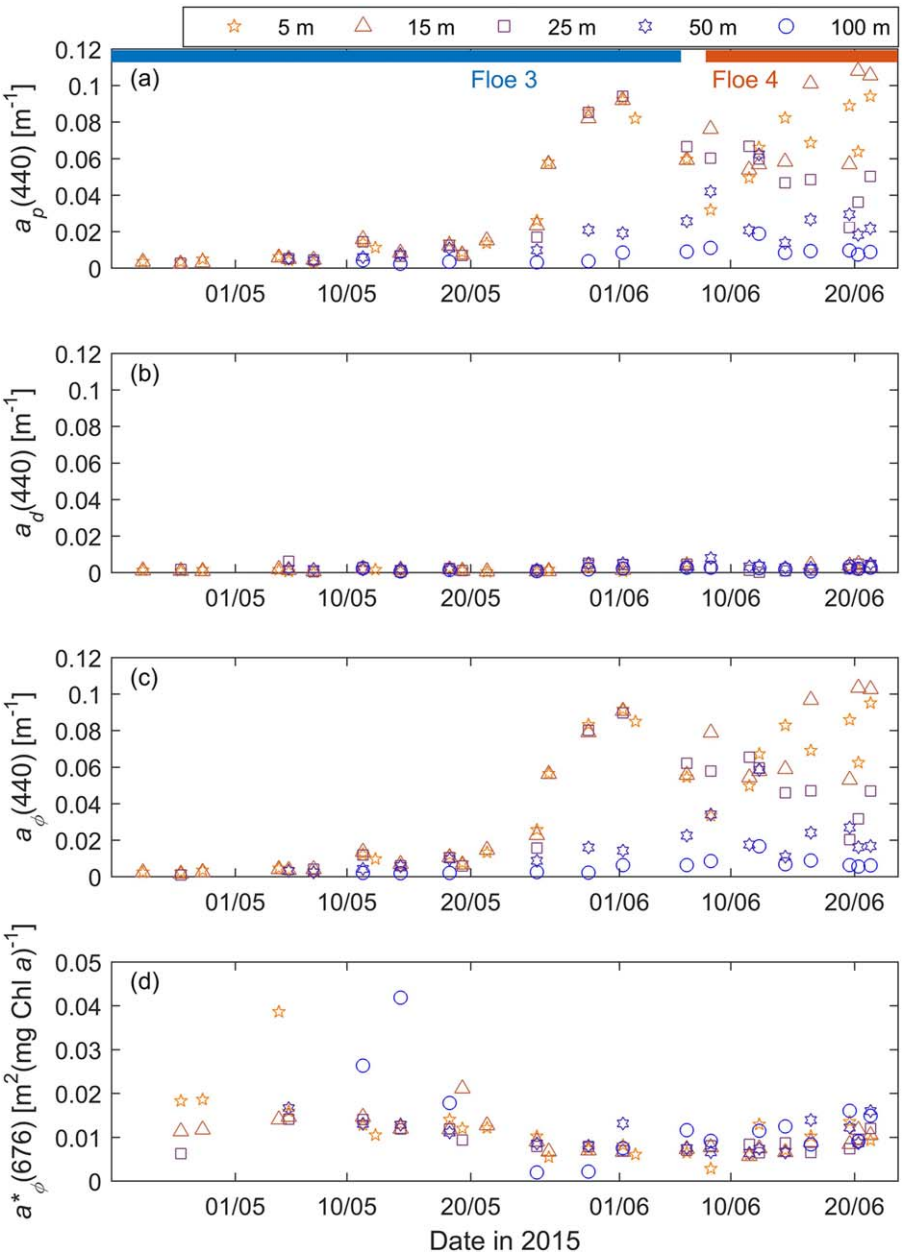

Figure 6. Evolution of (a) total particle absorption at 440 nm ($a_p(440)$); (b) detrital absorption at 440 nm ($a_d(440)$); (c) algal absorption at 440 nm ($a_\phi(440)$); (d) Chl *a* specific algal absorption at 676 nm ($a^*_\phi(676)$) at discrete sampling depths.

3.2. Effects of the Bloom on Under-Ice Light Field

Radiative transfer modeling has been known as a reliable way to estimate the underwater light field in aquatic environments and as an alternative to direct observations of $E_d(\lambda)$ and $E_o(\lambda)$ [e.g., *Mobley et al*., 1993; *Kirk*, 2011]. In ice-covered oceans, a challenge is that the light field under-ice with low transmittance can be influenced by light passing through neighboring ice with higher transmittance, such as melt ponds [*Frey et al*., 2011; *Katlein et al*., 2016]. At the ice bottom, the effect of a different transmittance can be seen within a distance of 2–3 times the ice thickness [*Ehn et al*., 2011; *Petrich et al*., 2012]. A plane parallel model is not able to capture such effects due to its 1-D nature [*Taskjelle et al*., 2017b]. Hence, while what happens immediately below the ice is likely well captured by AccuRT except for very close to the boundary between surface types, the discussion of what happens further down the water column may only be valid some longer distance from ice with notably different transmittance. Even in open water, the presence of waves and so-

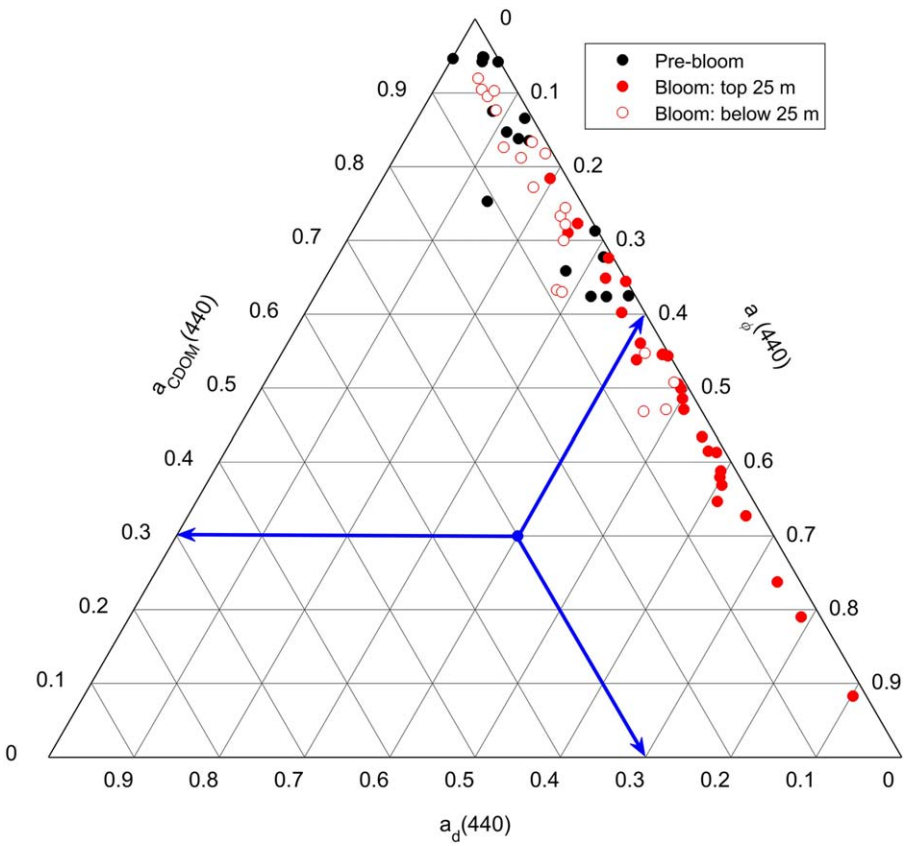

Figure 7. Relative contribution of CDOM, phytoplankton, and detritus to total nonwater light absorption at 440 nm for prebloom and bloom periods. Blue arrows are plotted to help reading and interpreting the graph.

called lens effects do not permit accurate measurements of $E_d(\lambda)$ or E_d(PAR) right below the surface [*Zaneveld et al*., 2001; *Antoine et al*., 2013]. Below we focus on two interesting features relevant for biological processes that emerged from our model simulations.

3.2.1. Scalar (Spherical) Versus Downwelling Planar Irradiance

Model simulations showed that the presence of sea ice and snow cover significantly affected absolute values of E_o(PAR) and E_d(PAR) in the surface layer for both "prebloom" and "bloom," as well as with the "*Pegau* turbid" settings [*Pegau*, 2002]. The latter setting was considered here for comparison (Figures 9a, 9c, and 9e). Under thin and thick ice, E_d(PAR) was reduced to 19% and $<$1% of incident E_d(PAR), respectively, which is consistent to in situ observations on both thin and thick ice during our campaign [*Assmy et al*., 2017; *Taskjelle et al*., 2017a; *Kauko et al*., 2017b] as well as previous works on light transmittance through Arctic sea ice

Table 4. Coefficients for Power Laws Expressed With an Equation (4) at 440 nm for Each of the Absorbing Components[a]

	A_p	B_p	r^2(p)	A_ϕ	B_ϕ	$r^2(\phi)$	A_d	B_d	r^2(d)	A_{CDOM}	B_{CDOM}	r^2(CDOM)	A_t	B_t	r^2(t)	N
This study (all)	0.0234	0.769	0.93	0.0206	0.828	0.93	0.0022	0.1107	0.11	0.0540	0.1159	0.12	0.0865	0.3485	0.69	167/70/59[b]
This study (pre-bloom)	0.0181	0.478	0.81	0.0195	0.676	0.90	0.0011	−0.1001	0.04	0.0263	−0.1044	0.45	0.0439	−0.0319	0.42	103/18/12[b]
This study (bloom)	0.0221	0.808	0.86	0.0197	0.858	0.87	0.0025	0.0543	0.01	0.0592	0.0733	0.04	0.0884	0.3378	0.64	64/52/47[b]
This study (bloom; top 25 m)	0.0224	0.796	0.66	0.0212	0.813	0.66	0.0013	0.4072	0.08	0.0690	−0.0434	0.00	0.0788	0.4079	0.37	38/30/27[b]
Matsuoka et al. [2007] (all depths)	0.0403	0.659	0.75	0.0288	0.820	0.80	0.0104	0.424	0.35	0.0858	0.167	0.14	0.14	0.281	0.43	183
Cota et al. [2003]	0.0542	0.544	0.80	0.0402	0.578	0.73	0.0151	0.410	0.55	0.0502	0.086	0.02				
Wang et al. [2005]	0.0511	0.585	0.79	0.0151	0.957	0.89	0.0306	0.296	0.41	0.0509	0.197	0.18				157
Bricaud et al. [1998]	0.0520	0.635	0.91	0.0378	0.627	0.90	0.0124	0.724	0.73							1166

[a]Available coefficients in the literature are presented for comparison. In *Bricaud et al*. [1998], the wavelength is 440 nm, while in other studies it is 443 nm.
[b]The number of samples is different for each component. First number is for $a_p(440)$, $a_\phi(440)$, and $a_d(440)$; second number is for $a_{CDOM}(440)$; third number is for total nonwater absorption (a).

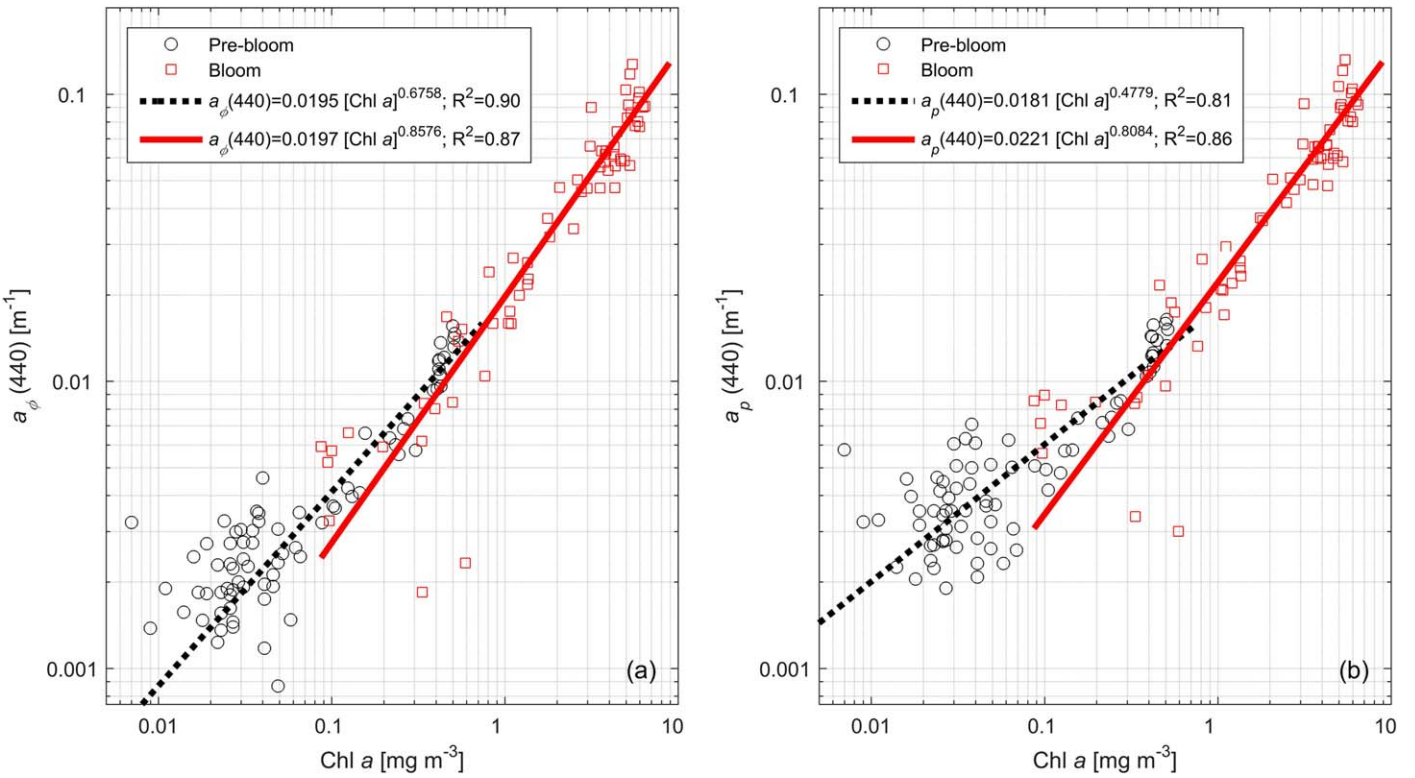

Figure 8. Relationships between absorption coefficients of (a) phytoplankton and (b) total particles and Chl *a*. Data are presented for the prebloom and bloom cases. Corresponding best power law fits are plotted and corresponding statistics are presented in Table 4.

[e.g., *Perovich*, 1996, 2005; *Nicolaus et al*., 2012]. For open water, the subsurface value of E_d(PAR) was about 94–95% of incident E_d(PAR).

Differences in absorption and scattering between IOPs settings (Table 2) affected the degree to which the light is attenuated in the water column (Figures 9a, 9c, and 9e). Below the bloom layer at 40 m depth, there was on average an order of magnitude difference in E_d(PAR) and E_o(PAR) between each of the three considered IOPs settings. Among the three IOPs settings, the strongest attenuation of PAR was seen during the bloom, the weakest before the bloom, with the "*Pegau* turbid" setting [*Pegau*, 2002] in between. Apparent attenuation was stronger in the top few meters, which is common in aquatic environments and reflects the strong absorption at longer wavelengths by pure water itself [*Kirk*, 2011].

As expected, values of scalar (spherical) irradiance, E_o(PAR) were consistently higher than E_d(PAR) throughout the upper 40 m of the water column. However, this difference is depth-dependent (Figures 9a, 9c, and 9e). To look closely at this feature, we show the ratio of E_o(PAR) to E_d(PAR) as a function of depth for three IOPs settings and surface type cases (Figures 9b, 9d, and 9f).

In open water, right below the sea surface E_o(PAR):E_d(PAR) was about 1.25 for the "Prebloom" and the "*Pegau* turbid" settings, and 1.30 for the "Bloom" case. Then E_o(PAR):E_d(PAR) gradually increased down to 8–10 m, and was thereafter relatively uniform down to 40 m. Such a vertical dependency of E_o:E_d ratio is known for open oceanic waters, and the ratio E_o(PAR):E_d(PAR) of 1.2 has been previously reported for surface waters [*Kirk*, 2011]. The general increase in E_o(PAR):E_d(PAR) is explained by the increasing diffusivity of the downwelling light field with depth, due to multiple scattering [*Kirk*, 2011]. This was clearly seen in the results of the high scattering "Bloom" setting, with E_o(PAR):E_d(PAR) values of 1.50–1.55 below 10 m, which is higher than for the "Prebloom" and "*Pegau* turbid" settings (Figure 9b). These relatively constant E_o(PAR):E_d(PAR) values below 10 m provide an indication that the asymptotic limit was reached during the highly-scattering "Bloom" scenario.

The highly diffuse light field below sea ice means the vertical variation of E_o(PAR):E_d(PAR) under-ice had a completely different shape than that in open water, with highest E_o(PAR):E_d(PAR) values of up to 1.85 right below the ice-ocean interface (Figures 9d and 9f). Below the ice E_o(PAR):E_d(PAR) rapidly decreased in the

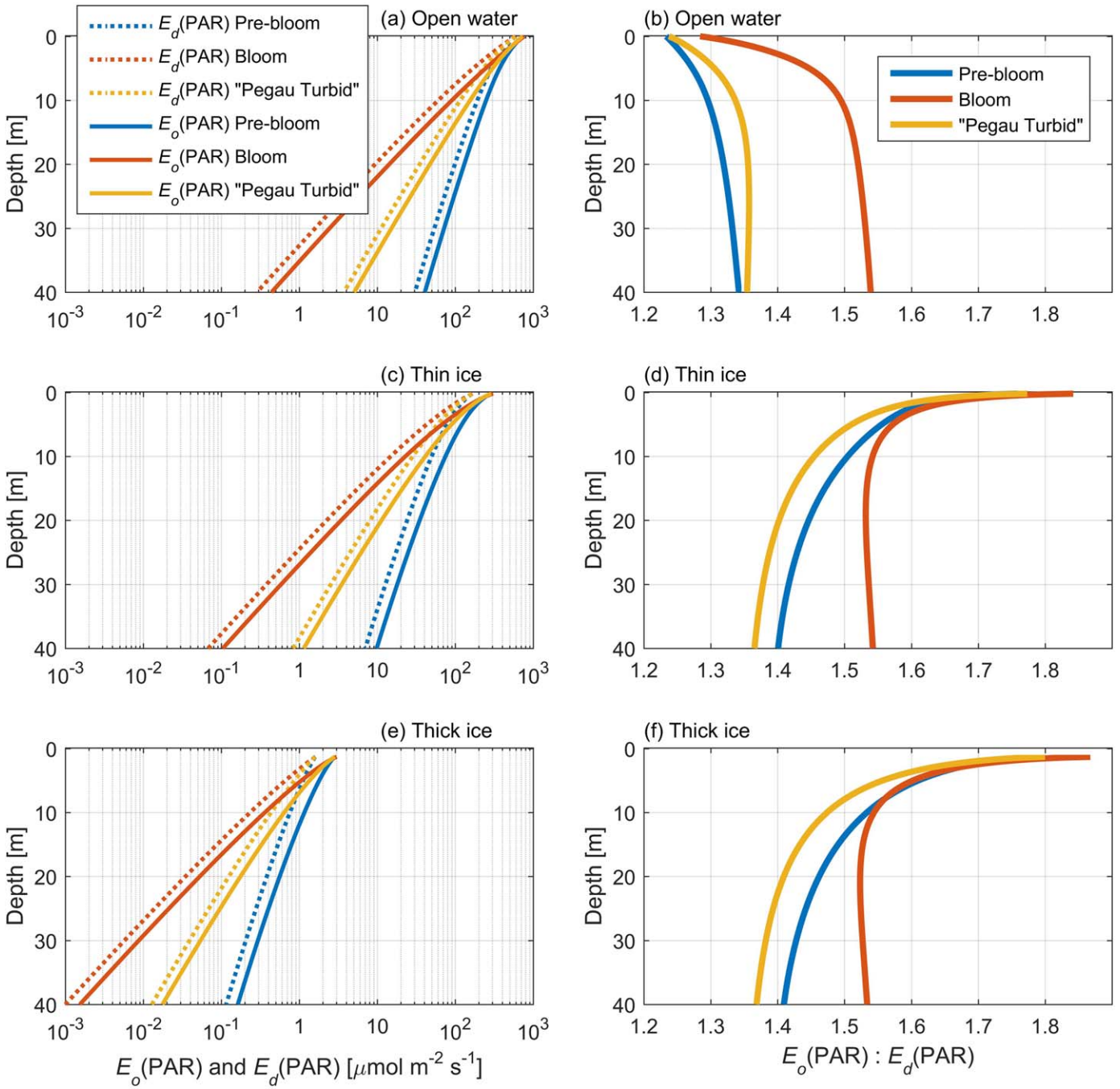

Figure 9. Examples of modeled vertical profiles of scalar E_o(PAR) and downwelling planar irradiance E_d(PAR) in the PAR range for (a) open water, (c) thin, and (e) thick ice cases. Vertical profiles of ratios of E_o(PAR) to E_d(PAR) under (b) open water, (d) thin ice, and (f) thick ice surface conditions. For all subplots, three cases of IOPs are considered: "Prebloom," "Bloom," "Pegau Turbid" [*Pegau*, 2002] (see Table 2).

upper 10 m, and then stood relatively uniform with values comparable to open water simulations. Previously, *Arst et al*. [2006] reported both similar depth dependence of the E_o(PAR):E_d(PAR) ratio as well as high E_o(PAR):E_d(PAR) values under lake ice and sea ice in the Baltic Sea ranging between 1.4 and 2.5, depending on surface properties of ice and optical properties of the water column. The only data under Arctic sea ice can be found in *Light et al*. [2015], who reported both scalar and downwelling planar irradiance values at one of the ice stations in the Beaufort Sea, from which E_o(PAR):E_d(PAR) of 1.94 (bare ice) and 1.72 (ponded ice) can be derived. There was no specific discussion about the E_o(PAR):E_d(PAR) ratio in this study.

Unfortunately, we do not have simultaneous measurements of E_o(PAR) and E_d(PAR) during our campaign, but some measurements of zenith radiance ($L_d(\lambda)$) and $E_d(\lambda)$ are available under thin ice at 10 m depth (not shown). The ratio of $L_d(\lambda)$:$E_d(\lambda)$ based on model simulations is higher during the bloom compared to in situ observations, thus, indicating a less isotropic light field in model simulations. This in turn would indicate that the E_o(PAR):E_d(PAR) ratio obtained from the model simulations is even lower than the in situ values.

One caveat to the model results is that the scattering coefficients ($b(\lambda)$) used within the sea ice in the model are independent of the direction in which light is travelling (i.e., scattering events are equally likely over a given distance, regardless of whether a light beam is propagating vertically, horizontally, or diagonally through the ice). *Katlein et al*. [2014] showed evidence that the scattering coefficients within sea ice are dependent on the direction of beam propagation, due to the frequently vertical columnar orientation of ice crystals and brine channels within sea ice. They showed that accounting for this effect results in a modeled downwelling radiance field just below the sea ice that decreases more rapidly with zenith angle than if the effect is not accounted for. As a result, our estimates of E_o(PAR):E_d(PAR) ratios below the sea ice might be slightly overestimated, though they are supported by previous in situ observations [*Arst et al*., 2006, 2008]. Importantly, we have not assumed an isotropic light field emerging from the bottom of the sea ice, which was the largest source of error highlighted by *Katlein et al*. [2014].

When it comes to biological implications, phototrophs (microalgae) are able to use light photons irrespective of the direction. Therefore, scalar (spherical) irradiance is generally recommended to be used in biological studies to characterize light availability for photosynthesis [*Mobley*, 1994; *Kirk*, 2011]. At the same time, downwelling planar irradiance is commonly measured above and below the ice, as it allows for estimating irradiance transmittance through the ice, which is further used for both physical and biological applications. At the moment, a number of Arctic (and Antarctic) primary production models developed for open water conditions use downwelling planar irradiance, as it is possible to obtain those values from satellite observations, climatology, and reanalysis products [e.g., *Arrigo et al*., 1998; *Babin et al*., 2015]. If similar concepts are used for ice-covered waters, it could significantly underestimate primary production estimates in the Arctic Ocean, and therefore modifications have to be used. The relationships between scalar and planar irradiances under the ice have been a subject to several recent studies [e.g., *Gradinger*, 2009; *Ehn and Mundy*, 2013; *Katlein et al*., 2014; *Fernández-Méndez et al*., 2015]. Based on our model runs, the E_o(PAR):E_d(PAR) ratio right below thick ice ranged between 1.79 and 1.87, and right below thin ice between 1.77 and 1.85. Hence the ratio was relatively independent of sea-ice and snow thickness and rather more dependent on optical properties of the water column, with higher scattering (and backscattering) likely explaining higher E_o(PAR) and, thus, E_o(PAR): E_d(PAR) ratio. A similar approach of correction factors between E_d(PAR) transmitted through the ice and E_o(PAR) based on AccuRT model simulations was implemented in *Assmy et al*. [2017], which helped to improve primary production estimates during the under-ice bloom described. Thus, our results are in line with previous works [*Gradinger*, 2009; *Ehn and Mundy*, 2013; *Katlein et al*., 2014; *Fernández-Méndez et al*., 2015] in highlighting the importance to distinguish between scalar and planar irradiances, and with a recommendation to use the former for primary production estimates. At the moment, a number of Arctic (and Antarctic) primary production models developed for open water conditions use downwelling planar irradiance, as it is possible to obtain those values from satellite observations, climatology, and reanalysis products [e.g., *Arrigo et al*., 1998; *Babin et al*., 2015]. If similar concepts are used for ice-covered waters, it could significantly underestimate primary production estimates in the Arctic Ocean, and therefore modifications have to be used.

3.2.2. Light Availability at the Ice-Ocean Interface

For most cases in ice-free natural waters, it is usually assumed that both scalar and planar irradiances decrease exponentially with depth in the absence of internal sources of light [e.g., *Mobley*, 1994; *Kirk*, 2011]. A number of recent studies have shown that in ice-covered waters a subsurface (5–10 m below the ice) increase in irradiance or radiance can be observed under highly heterogeneous ice covers, especially with melt ponds, with notably different light transmission [*Frey et al*., 2011; *Katlein et al*., 2014, 2016]. Another mechanism was suggested by *Leathers and McCormick* [1998], who showed, based on radiative transfer modeling, that scalar irradiance can exhibit a subsurface peak in some cases in the open ocean, especially in turbid waters when scattering to absorption ratio is high. *Leathers and McCormick* [1998] further hypothesized that a similar feature might be observed within and below the sea ice. However, they did not investigate this further and, apparently, this question has not gotten much

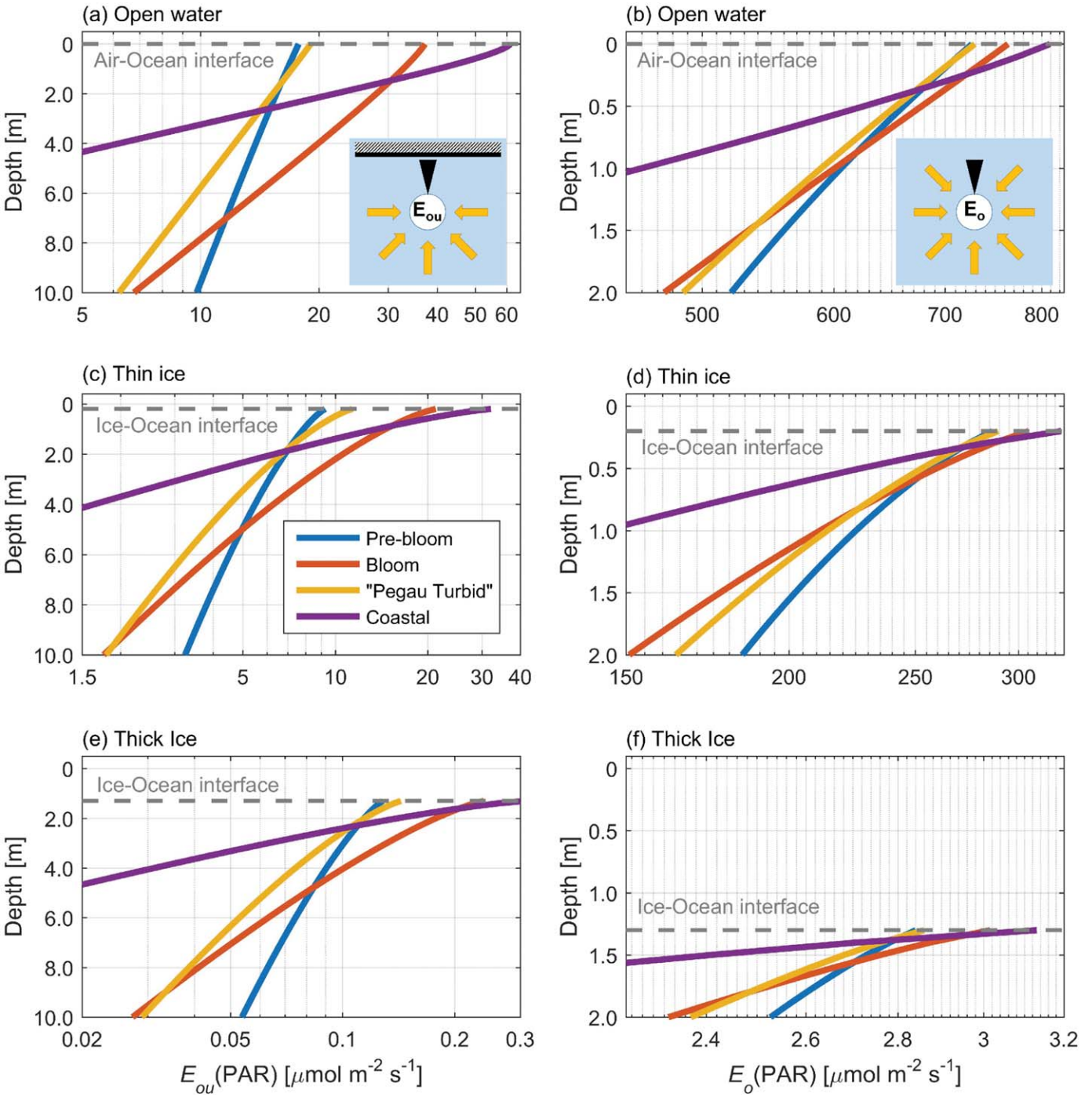

Figure 10. Examples of under-ice (underwater) profiles of upwelling scalar irradiance, (a, c, e) E_{ou}(PAR) and scalar (spherical) irradiance, (b, d, f) E_o(PAR) for (a, b) open water, (c, d) thin ice, and (e, f) thick ice surface conditions, considering four different IOPs settings: "Prebloom," "Bloom," "Pegau Turbid" [*Pegau*, 2002], and "Coastal" [*Hamre et al.*, 2003] (Table 2). Based on AccuRT model simulations.

attention. Similar features were observed in marine sediments, where a similar subsurface increase in scalar irradiance was observed within a thin layer of less 1 mm thick [*Kuhl et al.*, 1994]. A lack of observations of such phenomena in ice-covered waters can be explained by difficulties in conducting precise light measurements right underneath the ice (in top few centimeters) without affecting the light field. Even recent technological advances with a use of remotely operated vehicles (ROV) rarely allow light

measurements closer than 1 m from the ice-ocean interface, due to variable under-ice topography [e.g., *Nicolaus and Katlein*, 2013].

We investigated the effects of high scattering to absorption ratio (Figure 4) observed during the bloom on the light field at the ice-ocean interface using a radiative transfer model. Our simulations did not show a peak in E_o(PAR) under the ice. *Leathers and McCormick* [1998] pointed that this effect is strongest when the sun is at zenith and the illumination is direct. In our case, the solar zenith angle is relatively large (60°) and clouds are present that diffuse the light field, both of which would then reduce the effect. Strong scattering is required to see the effect, and the scattering observed during the bloom is likely not enough to overcome the limitations caused by the clouds and zenith angle. However, they showed a dependence of E_o(PAR) at the ice-ocean interface on optical properties of the underlying water column. Increased scattering in the water resulted in higher values of E_o(PAR) just below the sea ice under both thin and thick ice, and also just below the ocean surface for the open water case. We show examples of both the E_{ou}(PAR) and E_o(PAR) for the upper 10 and 2 m, respectively (Figure 10). These depth ranges were chosen to demonstrate vertical changes in E_{ou}(PAR) and E_o(PAR) in a best way.

Elevated scattering in the water column increases backscattering of light, thus resulting in higher values of upwelling irradiance (both scalar and planar). Relative to "prebloom" conditions, E_{ou}(PAR) at the ice-ocean interface doubled and tripled during the "bloom" and for the "coastal" setting (Figures 10a, 10c, and 10e). Since scalar irradiance is a sum of downwelling and upwelling components, a slight increase in E_o(PAR) was also seen (Figures 10b, 10d, and 10f). In relative numbers, under thin and thick ice there was an increase in E_o(PAR) of 6–7% and 10–13% for the "Bloom" and "Coastal" settings, relative to "Prebloom" conditions. This means, that in spite of the overall increase in absorption and scattering in the water column, and generally reduced levels of E_o(PAR) in the upper 40 m during the bloom (Figures 9a, 9c, and 9e), there was more PAR available at the ice-ocean interface.

Ehn and Mundy [2013] demonstrated that multiple scattering within the bottom ice layer can increase PAR availability, and thus, its absorption by ice algae. While focusing on sea-ice bottom layer, *Ehn and Mundy* [2013] considered only one case of relatively clear waters underneath the ice with Chl *a* concentrations of 0.01 mg m^{-3} and a scattering (backscattering) coefficient parameterized as a function of Chl *a* following *Morel and Maritorena* [2001]. At the same time, no high-scattering bottom layer was included in our model simulations, therefore direct comparisons between studies are difficult. However, our model results suggest that the ice-ocean interface and ice bottom layer can be exposed to even higher E_o(PAR) values, meaning that depending on optical properties in the water column light might be even less of a limiting factor for ice algae growth in early spring. Beyond cases of under-ice blooms, our findings would be relevant for some coastal Arctic waters influenced by turbid freshwater plumes (e.g., Mackenzie River) [*Doxaran et al*., 2012]) or coastal waters in glacial fjords [e.g., *Lund-Hansen et al*., 2012], where scattering coefficients can be an order of magnitude higher compared to our study [e.g., *Doxaran et al*., 2012].

4. Conclusions

We observed an extensive under-ice bloom of *Phaeocystis pouchetii* for 4 weeks in May–June 2015 in the Eurasian Basin of the Arctic Ocean [*Assmy et al*., 2017]. We documented a transition from relatively clear waters to opaque waters associated with the bloom (Figure 2). Prior the bloom CDOM dominated nonwater absorption at 440 nm. During the bloom, absorption in the visible range (440 nm) in the water column was dominated by phytoplankton and autochthonous CDOM, produced during the bloom. Contributions of detritus to total absorption were minor. The drastic increase in scattering was one of the characteristic features of the observed *Phaeocystis* bloom, which has several important effects on the under-ice light field as shown based on simulations with our 1-D coupled atmosphere-ice-ocean radiative transfer model (AccuRT).

The ratio of scalar (spherical) to downwelling planar irradiance, E_o(PAR):E_d(PAR), was up to 1.85 just below the sea ice, which is considerably higher compared to ice-free oceanic waters [e.g., *Kirk*, 2011]. Therefore, the use of E_d(PAR) for a parameterization of light in primary production models of ice-covered Arctic waters can significantly underestimate the amount of PAR available for photosynthesis and therefore predict lower primary productivity rates. Our findings about increased E_o(PAR) at the ice-ocean interface due to elevated scattering in the underlying water column during the bloom suggest a potential positive feedback on ice algae production. These results could also be relevant for analysis of under-ice light transmission

measurements [e.g., *Mundy et al*., 2007; *Nicolaus and Katlein*, 2013; *Campbell et al*., 2014]. Presence of a highly scattering phytoplankton bloom under the ice could affect the under-ice downwelling irradiance measurements, especially when the under-ice sensor is not placed immediately below the ice. Furthermore, our findings can be of interest together with the recent work by *Ehn and Mundy* [2013] showing that multiple scattering within the bottom ice layer can increase PAR availability for ice algae. In the future, a study looking at effects of both scattering in the ice bottom layer and underlying water column considering different seawater optical properties and ice-algal biomass scenarios would be noteworthy.

According to the complementary work by *Taskjelle et al*. [2017a], the bloom could cause a 0.2 K solar warming of the upper 10 m underneath the ice over a period of 25 days, heat that can be directly available for sea-ice melting. Based on results of these studies, we emphasize that a thorough description of IOPs (absorption and scattering) in the water column is important for correct description and parameterizations of the light field in ice-covered waters. This is particularly relevant as the occurrence of under-ice blooms could become more frequent under an increasingly thinner and more dynamic Arctic sea ice regime.

Acknowledgments

This work has been supported by the Centre for Ice, Climate and Ecosystems (ICE) at the Norwegian Polar Institute through the N-ICE project, and the Research Council of Norway through the STASIS project (221961/F20). A.K.P., M.A.G., and S.R.H. were supported by the Polish-Norwegian Research Programme operated by the National Centre for Research and Development under the Norwegian Financial Mechanism 2009–2014 in the frame of Project Contract Pol-Nor/197511/40/2013, CDOM-HEAT. H.M.K., M.A.G., P.A., and P.D. were funded by the Research Council of Norway (project Boom or Bust 244646/E10). C.J.M., M.F.M., and P.A. were supported by the Program Arktis 2030 (project ID Arctic) funded by the Ministry of Foreign Affairs and Ministry of Climate and Environment, Norway. C.J.M. was also supported through Natural Sciences and Engineering Research Council of Canada (NSERC) Discovery and Canada Foundation for Innovation grants. Authors thank crews of R/V Lance for help and assistance during the N-CE2015 expedition. We also thank Achim Randelhoff and Christine Provost for initial CTD data calibration and processing; Marcel Nicolaus for assistance with in situ measurements; Max König—for help with the map in Figure 1; the Norwegian Meteorological Institute and Polona Itkin for providing us with information on distance between the ice camp and open water; and Elina Nystedt and Colin Stedmon for laboratory measurements of particle absorption and CDOM. We thank Ciren Nima and Yi-Chun Chen for help with the particle absorption method and Jennifer King for help with interpretation of the radar image (Figure 1). The data used in this study have been deposited in the Norwegian Polar Data Centre (data.npolar.no).

References

Antoine, D., S. Hooker, S. Bélanger, A. Matsuoka, and M. Babin (2013), Apparent optical properties of the Canadian Beaufort Sea–Part 1: Observational overview and water column relationships, *Biogeosciences*, *10*(7), 4493–4509.

Arndt, S., and M. Nicolaus (2014), Seasonal cycle and long-term trend of solar energy fluxes through Arctic sea ice, *Cryosphere*, *8*(6), 2219–2233.

Arrigo, K. R., and G. L. van Dijken (2015), Continued increases in Arctic Ocean primary production, *Prog. Oceanogr.*, *136*, 60–70.

Arrigo, K. R., D. Worthen, A. Schnell, and M. P. Lizotte (1998), Primary production in Southern Ocean waters, *J. Geophys. Res.*, *103*(C8), 15,587–15,600.

Arrigo, K. R., et al. (2012), Massive phytoplankton blooms under Arctic sea ice, *Science*, *336*(6087), 1408–1408.

Arrigo, K. R., D. K. Perovich, R. S. Pickart, Z. W. Brown, G. L. van Dijken, K. E. Lowry, M. M. Mills, M. A. Palmer, W. M. Balch, and N. R. Bates (2014), Phytoplankton blooms beneath the sea ice in the Chukchi Sea, *Deep Sea Res., Part II*, *105*, 1–16.

Arst, H., A. Erm, M. Leppäranta, and A. Reinart (2006), Radiative characteristics of ice-covered fresh-and brackish-water bodies, *Proc. Estonian Acad. Sci. Geol.*, *55*(1), 3–23.

Arst, H., T. Noges, P. Noges, and B. Paavel (2008), Relations of phytoplankton in situ primary production, chlorophyll concentration and underwater irradiance in turbid lakes, *Hydrobiologia*, *599*(1), 169–176.

Assmy, P., et al. (2017), Leads in Arctic pack ice enable early phytoplankton blooms below snow-covered sea ice, *Sci. Rep.*, *7*, 40850, doi:10.1038/srep40850.

Babin, M., Morel, A., Fournier-Sicre, V., Fell, F., and D. Stramski (2003), Light scattering properties of marine particles in coastal and open ocean waters as related to particle mass concentration, *Limnol. Oceanogr.*, *48*(2), 843–859.

Babin, M., S. Bélanger, I. Ellingsen, A. Forest, V. Le Fouest, T. Lacour, M. Ardyna, and D. Slagstad (2015), Estimation of primary production in the Arctic Ocean using ocean colour remote sensing and coupled physical–biological models: Strengths, limitations and how they compare, *Prog. Oceanogr.*, *139*, 197–220.

Balch, W., B. Bowler, L. Lubelczyk, and M. Stevens (2014), Aerial extent, composition, bio-optics and biogeochemistry of a massive under-ice algal bloom in the Arctic, *Deep Sea Res. Part II*, *105*, 42–58.

Barber, D. G., et al. (2015), Selected physical, biological and biogeochemical implications of a rapidly changing Arctic Marginal Ice Zone, *Prog. Oceanogr.*, *139*, 122–150.

Bélanger, S., J. K. Ehn, and M. Babin (2007), Impact of sea ice on the retrieval of water-leaving reflectance, chlorophyll a concentration and inherent optical properties from satellite ocean color data, *Remote Sens. Environ.*, *111*(1), 51–68.

Bélanger, S., S. Cizmeli, J. Ehn, A. Matsuoka, D. Doxaran, S. Hooker, and M. Babin (2013), Light absorption and partitioning in Arctic Ocean surface waters: Impact of multiyear ice melting, *Biogeosciences*, *10*(10), 6433–6452.

Bricaud, A., A. Morel, M. Babin, K. Allali, and H. Claustre (1998), Variations of light absorption by suspended particles with chlorophyll a concentration in oceanic (case 1) waters: Analysis and implications for bio-optical models, *J. Geophys. Res.*, *103*(C13), 31,033–31,044.

Cleveland, W. S. (1979), Robust locally weighted regression and smoothing scatterplots, *J. Am. Stat. Assoc.*, *74*(368), 829–836.

Cohen, L., S. Hudson, V. Walden, R. Graham, and M. Granskog (2017), Meteorological conditions in a thinner Arctic sea ice regime from winter through summer during the Norwegian Young Sea Ice expedition (N-ICE2015), *J. Geophys. Atmos.*, *122*, doi:10.1002/2016JD026034, in press.

Cota, G. F., W. G. Harrison, T. Platt, S. Sathyendranath, and V. Stuart (2003), Bio-optical properties of the Labrador Sea, *J. Geophys. Res.*, *108*(C7), 3228, doi:10.1029/2000JC000597.

Doxaran, D., J. Ehn, S. Bélanger, A. Matsuoka, S. Hooker, and M. Babin (2012), Optical characterization of suspended particles in the Mackenzie River plume (Canadian Arctic Ocean) and implications for ocean color remote sensing, *Biogeosciences*, *9*(8), 3213–3229.

Ehn, J. K., and C. Mundy (2013), Assessment of light absorption within highly scattering bottom sea ice from under-ice light measurements: Implications for Arctic ice algae primary production, *Limnol. Oceanogr.*, *58*(3), 893–902.

Ehn, J. K., C. J. Mundy, D. G. Barber, H. Hop, A. Rossnagel, and J. Stewart (2011), Impact of horizontal spreading on light propagation in melt pond covered seasonal sea ice in the Canadian Arctic, *J. Geophys. Res.*, *116*, C00G02, doi:10.1029/2010JC006908.

Falkowski, P. G. (1980), Light-shade adaptation in marine phytoplankton, In *Primary Productivity in the Sea*, pp. 99–119, Springer, New York.

Fernández-Méndez, M., C. Katlein, B. Rabe, M. Nicolaus, I. Peeken, K. Bakker, H. Flores, and A. Boetius (2015), Photosynthetic production in the central Arctic Ocean during the record sea-ice minimum in 2012, *Biogeosciences*, *12*(11), 3525–3549.

Fortier, M., L. Fortier, C. Michel, and L. Legendre (2002), Climatic and biological forcing of the vertical flux of biogenic particles under seasonal Arctic sea ice, *Mar. Ecol. Prog. Ser.*, *225*, 1–16.

Frey, K. E., D. K. Perovich, and B. Light (2011), The spatial distribution of solar radiation under a melting Arctic sea ice cover, *Geophys. Res. Lett.*, *38*, L22501, doi:10.1029/2011GL049421.

Gjerstad, K. I., J. J. Stamnes, B. Hamre, J. K. Lotsberg, B. Yan, and K. Stamnes (2003), Monte Carlo and discrete-ordinate simulations of irradiances in the coupled atmosphere-ocean system, *Appl. Opt.*, *42*(15), 2609–2622.

Gradinger, R. (2009), Sea-ice algae: Major contributors to primary production and algal biomass in the Chukchi and Beaufort Seas during May/June 2002, *Deep Sea Res. Part II*, *56*(17), 1201–1212.
Granskog, M. A., R. W. Macdonald, C.-J. Mundy, and D. G. Barber (2007), Distribution, characteristics and potential impacts of chromophoric dissolved organic matter (CDOM) in Hudson Strait and Hudson Bay, Canada, *Cont. Shelf Res.*, *27*(15), 2032–2050.
Granskog, M. A., C. A. Stedmon, P. A. Dodd, R. M. Amon, A. K. Pavlov, L. Steur, and E. Hansen (2012), Characteristics of colored dissolved organic matter (CDOM) in the Arctic outflow in the Fram Strait: Assessing the changes and fate of terrigenous CDOM in the Arctic Ocean, *J. Geophys. Res.*, *117*, C12021, doi:10.1029/2012JC008075.
Granskog, M. A., A. K. Pavlov, S. Sagan, P. Kowalczuk, A. Raczkowska, and C. A. Stedmon (2015), Effect of sea-ice melt on inherent optical properties and vertical distribution of solar radiant heating in Arctic surface waters, *J. Geophys. Res. Oceans*, *120*, 7028–7039, doi:10.1002/2015JC011087.
Granskog, M. A., P. Assmy, S. Gerland, G. Spreen, H. Steen, and L. Smedsrud (2016), Arctic research on thin ice: Consequences of Arctic sea ice loss, *Eos*, *97*, 22–26, doi:10.1029/2016EO044097.
Hamm, C. E., D. A. Simson, R. Merkel, and V. Smetacek (1999), Colonies of *Phaeocystis globosa* are protected by a thin but tough skin, *Mar. Ecol. Prog. Ser.*, *187*, 101–111.
Hamre, B., Ø. Frette, S. R. Erga, J. J. Stamnes, and K. Stamnes (2003), Parameterization and analysis of the optical absorption and scattering coefficients in a western Norwegian fjord: A case II water study, *Appl. Opt.*, *42*(6), 883–892.
Hamre, B., J. G. Winther, S. Gerland, J. J. Stamnes, and K. Stamnes (2004), Modeled and measured optical transmittance of snow-covered first-year sea ice in Kongsfjorden, Svalbard, *J. Geophys. Res.*, *109*, C10006, doi:10.1029/2003JC001926.
Hancke, K., E. K. Hovland, Z. Volent, R. Pettersen, G. Johnsen, M. Moline, and E. Sakshaug (2014), Optical properties of CDOM across the Polar Front in the Barents Sea: Origin, distribution and significance, *J. Mar. Syst.*, *130*, 219–227.
Helms, J. R., A. Stubbins, J. D. Ritchie, E. C. Minor, D. J. Kieber, and K. Mopper (2008), Absorption spectral slopes and slope ratios as indicators of molecular weight, source, and photobleaching of chromophoric dissolved organic matter, *Limnol. Oceanogr.*, *53*(3), 955–969.
Hill, V. J. (2008), Impacts of chromophoric dissolved organic material on surface ocean heating in the Chukchi Sea, *J. Geophys. Res.*, *113*, C07024, doi:10.1029/2007JC004119.
Hill, V. J., P. A. Matrai, E. Olson, S. Suttles, M. Steele, L. Codispoti, and R. C. Zimmerman (2013), Synthesis of integrated primary production in the Arctic Ocean: II. In situ and remotely sensed estimates, *Prog. Oceanogr.*, *110*, 107–125.
Holm-Hansen, O., and B. Riemann (1978), Chlorophyll a determination: Improvements in methodology, *Oikos*, *30*, 438–447.
Johnsen, G., O. Samset, L. Granskog, and E. Sakshaug (1994), In-vivo absorption characteristics in 10 classes of bloom-forming phytoplankton-taxonomic characteristics and responses to photoadaptation by means of discriminant and HPLC analysis, *Mar. Ecol. Prog. Ser.*, *105*(1-2), 149–157.
Katlein, C., M. Nicolaus, and C. Petrich (2014), The anisotropic scattering coefficient of sea ice, *J. Geophys. Res. Oceans*, *119*, 842–855, doi: 10.1002/2013JC009502.
Katlein, C., D. K. Perovich, and M. Nicolaus (2016), Geometric effects of an inhomogeneous sea ice cover on the under ice light field, *Front. Earth Sci.*, *4*, 6.
Kauko, H. M., A. K. Pavlov, E. Nystedt, and M. Granskog (2017a), N-ICE2015 particulate matter absorption spectra [Data set]. Norw. Polar Inst., Tromsø, Norway, doi: 10.21334/npolar.2017.35978199.
Kauko, H. M., et al. (2017b), Windows in Arctic sea ice: Light transmission and ice algal optical properties in a refrozen lead, *J. Geophys. Res. Biogeosci.*, *122*, doi:10.1002/2016JG003626, in press.
Kieber, D. J., D. A. Toole, and R. P. Kiene (2009), Chromophoric dissolved organic matter cycling during a Ross Sea Phaeocystis Antarctica bloom, In *Smithsonian at the Poles: Contributions to International Polar Year Science*, edited by I. Krupnik, M. A. Lang, and S. E. Miller, pp. 309–318, Smithsonian Inst. Sch. Press, Washington, D. C.
Kirk, J. T. (2011), *Light and Photosynthesis in Aquatic Ecosystems*, 3rd ed., Cambridge Univ. Press, Cambridge, U. K.
Kuhl, M., C. Lassen, and B. Jørgensen (1994), Light penetration and light-intensity in sandy marine-sediments measured with irradiance and scalar irradiance fiber optic microprobes, *Mar. Ecol. Prog. Ser.*, *105*, 139–148.
Kwok, R. (2009), Outflow of Arctic Ocean sea ice into the Greenland and Barents Seas: 1979–2007, *J. Clim.*, *22*(9), 2438–2457.
Leathers, R., and N. J. McCormick (1998), Ocean scalar irradiance near-surface maxima, *Limnol. Oceanogr.*, *43*(5), 982–986.
Lee, S. H., D. Stockwell, and T. E. Whitledge (2010), Uptake rates of dissolved inorganic carbon and nitrogen by under-ice phytoplankton in the Canada Basin in summer 2005, *Polar Biol.*, *33*(8), 1027–1036.
Leu, E., C. Mundy, P. Assmy, K. Campbell, T. Gabrielsen, M. Gosselin, T. Juul-Pedersen, and R. Gradinger (2015), Arctic spring awakening–steering principles behind the phenology of vernal ice algal blooms, *Prog. Oceanogr.*, *139*, 151–170.
Light, B., D. K. Perovich, M. A. Webster, C. Polashenski, and R. Dadic (2015), Optical properties of melting first-year Arctic sea ice, *J. Geophys. Res. Oceans*, *120*, 7657–7675, doi:10.1002/2015JC011163.
Logvinova, C. L., K. E. Frey, and L. W. Cooper (2016), The Potential Role of Sea Ice Melt in the Distribution of Chromophoric Dissolved Organic Matter in the Chukchi and Beaufort Seas, *Deep Sea Res., Part II*, *130*, 28–42, doi:10.1016/j.dsr2.2016.04.017.
Lund-Hansen, L. C., S. Markager, K. Hancke, T. Stratmann, S. Rysgaard, H. Ramløv, and B. K. Sorrell (2015), Effects of sea-ice light attenuation and CDOM absorption in the water below the Eurasian sector of central Arctic Ocean (> 88° N), *Polar Res.*, *34*, 23978.
Matsuoka, A., Y. Huot, K. Shimada, S.-I. Saitoh, and M. Babin (2007), Bio-optical characteristics of the western Arctic Ocean: Implications for ocean color algorithms, *Can. J. Remote Sens.*, *33*(6), 503–518.
Matsuoka, A., V. Hill, Y. Huot, M. Babin, and A. Bricaud (2011), Seasonal variability in the light absorption properties of western Arctic waters: Parameterization of the individual components of absorption for ocean color applications, *J. Geophys. Res.*, *116*, C02007, doi:10.1029/2009JC005594.
Matsuoka, A., A. Bricaud, R. Benner, J. Para, R. Sempéré, L. Prieur, S. Bélanger, and M. Babin (2012), Tracing the transport of colored dissolved organic matter in water masses of the Southern Beaufort Sea: Relationship with hydrographic characteristics, *Biogeosciences*, *9*(3), 925–940.
Matsuoka, A., M. Babin, D. Doxaran, S. B. Hooker, B. G. Mitchell, S. Bélanger, and A. Bricaud (2014), A synthesis of light absorption properties of the Arctic Ocean: Application to semianalytical estimates of dissolved organic carbon concentrations from space, *Biogeosciences*, *11*(12), 3131–3147.
Matsuoka, A., E. Ortega-Retuerta, A. Bricaud, K. R. Arrigo, and M. Babin (2015), Characteristics of colored dissolved organic matter (CDOM) in the Western Arctic Ocean: Relationships with microbial activities, *Deep Sea Res., Part II*, *118*, 44–52.
Meier, W. N., et al. (2014), Arctic sea ice in transformation: A review of recent observed changes and impacts on biology and human activity, *Rev. Geophys.*, *52*, 185–217, doi:10.1002/2013RG000431.
Meyer, A., et al. (2017), Winter to summer oceanographic observations in the Arctic Ocean north of Svalbard, *J. Geophys. Res. Oceans*, doi: 10.1002/2016JC012391, in press.
Mobley, C. D. (1994), *Light and Water: Radiative Transfer in Natural Waters*, Academic, San Diego, Calif.

Mobley, C. D., B. Gentili, H. R. Gordon, Z. Jin, G. W. Kattawar, A. Morel, P. Reinersman, K. Stamnes, and R. H. Stavn (1993), Comparison of numerical models for computing underwater light fields, *Appl. Opt.*, *32*(36), 7484–7504.

Moisan, T. A., and B. G. Mitchell (1999), Photophysiological acclimation of Phaeocystis Antarctica Karsten under light limitation, *Limnol. Oceanogr.*, *44*(2), 247–258.

Morel, A., and A. Bricaud (1981), Theoretical results concerning light absorption in a discrete medium, and application to specific absorption of phytoplankton, *Deep Sea Res., Part A*, *28*(11), 1375–1393.

Morel, A., and S. Maritorena (2001), Bio-optical properties of oceanic waters: A reappraisal, *J. Geophys. Res.*, *106*(C4), 7163–7180.

Mueller, J. L., G. S. Fargion, C. R. McClain, S. Pegau, J. R. V. Zanefeld, B. G. Mitchell, M. Kahru, J. Wieland, and M. Stramska (2003), Ocean Optics Protocols for Satellite Ocean Color Sensor Validation, Revision 4, Volume IV: Inherent Optical Properties: Instruments, Characterizations, Field Measurements and Data Analysis Protocols, NASA Technical Reports, NASA Goddard Space Flight Center, Greenbelt, Md.

Mundy, C., J. Ehn, D. Barber, and C. Michel (2007), Influence of snow cover and algae on the spectral dependence of transmitted irradiance through Arctic landfast first-year sea ice, *J. Geophys. Res.*, *112*, C03007, doi:10.1029/2006JC003683.

Mundy, C., M. Gosselin, J. Ehn, Y. Gratton, A. Rossnagel, D. G. Barber, J. Martin, J. É. Tremblay, M. Palmer, and K. R. Arrigo (2009), Contribution of under-ice primary production to an ice-edge upwelling phytoplankton bloom in the Canadian Beaufort Sea, *Geophys. Res. Lett.*, *36*, L17601, doi:10.1029/2009GL038837.

Mundy, C., M. Gosselin, Y. Gratton, K. Brown, V. Galindo, K. Campbell, M. Levasseur, D. Barber, T. Papakyriakou, and S. Bélanger (2014), Role of environmental factors on phytoplankton bloom initiation under landfast sea ice in Resolute Passage, Canada, *Mar. Ecol. Prog. Ser.*, *497*, 39–49.

Nelson, N. B., D. A. Siegel, and A. F. Michaels (1998), Seasonal dynamics of colored dissolved material in the Sargasso Sea, *Deep Sea Res. Part I*, *45*(6), 931–957.

Neukermans, G., R. A. Reynolds, and D. Stramski (2014), Contrasting inherent optical properties and particle characteristics between an under-ice phytoplankton bloom and open water in the Chukchi Sea, *Deep Sea Res. Part II*, *105*, 59–73.

Neukermans, G., R. A. Reynolds, and D. Stramski (2016), Optical classification and characterization of marine particle assemblages within the western Arctic Ocean, *Limnol. Oceanogr.*, *61*(4), 1472–1494.

Nicolaus, M., and C. Katlein (2013), Mapping radiation transfer through sea ice using a remotely operated vehicle (ROV), *Cryosphere*, *7*(3), 763–777.

Nicolaus, M., C. Katlein, J. Maslanik, and S. Hendricks (2012), Changes in Arctic sea ice result in increasing light transmittance and absorption, *Geophys. Res. Lett.*, *39*, L24501, doi:10.1029/2012GL053738.

Nicolaus, M., C. Petrich, S. R. Hudson, and M. A. Granskog (2013), Variability of light transmission through Arctic land-fast sea ice during spring, *Cryosphere*, *7*, 977–986, doi:10.5194/tc-7-977-2013.

Pavlov, A. K., A. Silyakova, M. A. Granskog, R. G. Bellerby, A. Engel, K. G. Schulz, and C. P. Brussaard (2014), Marine CDOM accumulation during a coastal Arctic mesocosm experiment: No response to elevated pCO2 levels, *J. Geophys. Res. Biogeosciences*, *119*, 1216–1230, doi: 10.1002/2013JG002587.

Pavlov, A. K., M. A. Granskog, C. A. Stedmon, B. V. Ivanov, S. R. Hudson, and S. Falk-Petersen (2015), Contrasting optical properties of surface waters across the Fram Strait and its potential biological implications, *J. Mar. Syst.*, *143*, 62–72, doi:10.1016/j.jmarsys.2014.11.001.

Pavlov, A. K., T. Taskjelle, S. Hudson, B. Hamre, and M. A. Granskog (2016a), N-ICE2015 total absorption profiles from water column [Data set], Norw. Polar Inst., Tromsø, Norway, doi:10.21334/npolar.2017.7dce5c52.

Pavlov, A. K., C. A. Stedmon, A. V. Semushin, T. Martma, B. V. Ivanov, P. Kowalczuk, and M. A. Granskog (2016b), Linkages between the circulation and distribution of dissolved organic matter in the White Sea, Arctic Ocean, *Cont. Shelf Res.*, *119*, 1–13.

Pavlov, A. K., H. M. Kauko, C. Stedmon, and M. Granskog (2017), N-ICE2015 colored dissolved organic matter absorption spectra [Data set], Norw. Polar Inst., Tromsø, Norway, doi: 10.21334/npolar.2017.f46970ba.

Pegau, W. S. (2002), Inherent optical properties of the central Arctic surface waters, *J. Geophys. Res.*, *107*(C10), 8035, doi:10.1029/2000JC000382.

Perovich, D. K. (1996), The Optical Properties of Sea Ice, *CRREL Monogr.*, 96-1, 1–23, Hanover, N. H.

Perovich, D. K. (2005), On the aggregate-scale partitioning of solar radiation in Arctic sea ice during the Surface Heat Budget of the Arctic Ocean (SHEBA) field experiment, *J. Geophys. Res.*, *110*, C03002, doi:10.1029/2004JC002512.

Petrich, C., M. Nicolaus, and R. Gradinger (2012), Sensitivity of the light field under sea ice to spatially inhomogeneous optical properties and incident light assessed with three-dimensional Monte Carlo radiative transfer simulations, *Cold Reg. Sci. Technol.*, *73*, 1–11.

Pope, R. M., and E. S. Fry (1997), Absorption spectrum (380–700 nm) of pure water. II. Integrating cavity measurements, *Appl. Opt.*, *36*(33), 8710–8723.

Popova, E. E., A. Yool, A. C. Coward, F. Dupont, C. Deal, S. Elliott, E. Hunke, M. Jin, M. Steele, and J. Zhang (2012), What controls primary production in the Arctic Ocean? Results from an intercomparison of five general circulation models with biogeochemistry, *J. Geophys. Res.*, *117*, C00D12, doi:10.1029/2011JC007112.

Provost, C., Sennéchael, N., Miguet, J., Itkin, P., Rösel, A., Koenig, Z., Villacieros-Robineau, N. and Granskog, M.A. (2017), Observations of flooding and snow-ice formation in a thinner Arctic sea ice regime during the N-ICE2015 campaign: Influence of basal ice melt and storms, *J. Geophys. Res. Oceans*, doi:10.1002/2016JC012011, in press.

Röttgers, R., D. McKee, and C. Utschig (2014), Temperature and salinity correction coefficients for light absorption by water in the visible to infrared spectral region, *Opt. Express*, *22*(21), 25,093–25,108.

Rudels, B. (1989), The formation of Polar Surface Water, the ice export and the exchanges through the Fram Strait, *Prog. Oceanogr.*, *22*(3), 205–248.

Rudels, B., M. Korhonen, U. Schauer, S. Pisarev, B. Rabe, and A. Wisotzki (2015), Circulation and transformation of Atlantic water in the Eurasian Basin and the contribution of the Fram Strait inflow branch to the Arctic Ocean heat budget, *Prog. Oceanogr.*, *132*, 128–152.

Sakshaug, E., and O. Holm-Hansen (1984), Factors governing pelagic production in polar oceans, in *Marine Phytoplankton and Productivity*, edited by O. Holm-Hansen, L. Bolis, and R. Gilles, pp. 1–18, Springer-Verlag, New York.

Segelstein, D. J. (1981), The complex refractive index of water, doctoral dissertation, Univ. of Missouri-Kansas, Kansas. [Available at http://hdl.handle.net/10355/11599.]

Sherr, E. B., B. F. Sherr, P. A. Wheeler, and K. Thompson (2003), Temporal and spatial variation in stocks of autotrophic and heterotrophic microbes in the upper water column of the central Arctic Ocean, *Deep Sea Res., Part I*, *50*(5), 557–571.

Slagstad, D., I. Ellingsen, and P. Wassmann (2011), Evaluating primary and secondary production in an Arctic Ocean void of summer sea ice: An experimental simulation approach, *Prog. Oceanogr.*, *90*(1), 117–131.

Slagstad, D., P. F. Wassmann, and I. Ellingsen (2015), Physical constrains and productivity in the future Arctic Ocean, *Front. Mar. Sci.*, *2*, 85.

Smith, R. C., and K. S. Baker (1981), Optical properties of the clearest natural waters (200–800 nm), *Appl. Opt.*, *20*(2), 177–184.

Sogandares, F. M., and E. S. Fry (1997), Absorption spectrum (340–640 nm) of pure water: I. Photothermal measurements, *Appl. Opt.*, *36*(33), 8699–8709.

Stamnes, K., B. Hamre, J.J. Stamnes, G. Ryzhikov, M. Biryulina, R. Mahoney, B. Hauss, and A. Sei (2011), Modeling of radiation transport in coupled atmosphere-snow-ice-ocean systems, *J. Quant. Spectrosc. Radiat. Transfer*, *112*(4), 714–726, doi:10.1016/j.jqsrt.2010.06.006.

Stedmon, C., and S. Markager (2001), The optics of chromophoric dissolved organic matter (CDOM) in the Greenland Sea: An algorithm for differentiation between marine and terrestrially derived organic matter, *Limnol. Oceanogr.*, *46*(8), 2087–2093.

Stedmon, C., S. Markager, and H. Kaas (2000), Optical properties and signatures of chromophoric dissolved organic matter (CDOM) in Danish coastal waters, *Estuarine Coastal Shelf Sci.*, *51*(2), 267–278.

Taskjelle, T., M. A. Granskog, A. K. Pavlov, S. Hudson, and B. Hamre (2016a), N-ICE2015 total attenuation and absorption profiles from water column with AC-9, Norw. Polar Inst., Tromsø, Norway, doi:10.21334/npolar.2016.114bfaaa.

Taskjelle, T., S. R. Hudson, M. A. Granskog, M. Nicolaus, R. Lei, S. Gerland, J. J. Stamnes, and B. Hamre (2016b), Spectral albedo and transmittance of thin young Arctic sea ice, *J. Geophys. Res. Oceans*, *121*, 540–553, doi:10.1002/2015JC011254.

Taskjelle, T., M. A. Granskog, A. K. Pavlov, S. R. Hudson, and B. Hamre (2017a), Effects of an Arctic under-ice bloom on solar radiant heating of the water column, *J. Geophys. Res. Oceans*, *122*, 126–138, doi:10.1002/2016JC012187.

Taskjelle, T., Hudson, S.R., Granskog, M.A. and Hamre, B. (2017b), Modelling radiative transfer through ponded first-year Arctic sea ice with a plane parallel model, *Cryosphere Discuss.*, doi:10.5194/tc-2017-36.

Tassan, S., and G. Ferrari (2002), A sensitivity analysis of the 'Transmittance–Reflectance' method for measuring light absorption by aquatic particles, *J. Plankton Res.*, *24*(8), 757–774.

Thomas, G. E., and K. Stamnes (2002), *Radiative Transfer in the Atmosphere and Ocean*, Cambridge Univ. Press, Cambridge, U. K.

Tilstone, G., G. Moore, K. Sørensen, R. Doerfeer, R. Røttgers, K. Ruddick, R. Pasterkamp, and P. Jørgensen (2002), Regional validation of MERIS chlorophyll products in North Sea coastal waters, *REVAMP Methodol. EVGI-CT-2001-00049*, pp. 1–77, Dev. of Generic Earth Observ. Technol., Paris.

Tremblay, J.-É., and J. Gagnon (2009), The effects of irradiance and nutrient supply on the productivity of Arctic waters: A perspective on climate change, in *Influence of Climate Change on the Changing Arctic and Sub-arctic Conditions*, edited by J. C. J. Nihoul, A. G. Kostianoy, pp. 73–93, Springer, Dordrecht.

Vancoppenolle, M., L. Bopp, G. Madec, J. Dunne, T. Ilyina, P. R. Halloran, and N. Steiner (2013), Future Arctic Ocean primary productivity from CMIP5 simulations: Uncertain outcome, but consistent mechanisms, *Global Biogeochem. Cycles*, *27*, 605–619, doi:10.1002/gbc.20055.

Von Quillfeldt, C. H. (2000), Common diatom species in Arctic spring blooms: Their distribution and abundance, *Bot. Mar.*, *43*(6), 499–516.

Wang, J., G. F. Cota, and D. A. Ruble (2005), Absorption and backscattering in the Beaufort and Chukchi Seas, *J. Geophys. Res.*, *110*, C04014, doi:10.1029/2002JC001653.

Warren, S.G. and R.E. Brandt (2008), Optical constants of ice from the ultraviolet to the microwave: A revised compilation, *J. Geophys. Res.*, *113*, D14220, doi:10.1029/2007JD009744.

Zaneveld, J. R. V., J. C. Kitchen, and C. C. Moore (1994), Scattering error correction of reflecting-tube absorption meters, paper presented at Ocean Optics XII, Int. Soc. for Opt. and Photon., Bellingham, Wash.

Zaneveld, J. R. V., E. Boss, and A. Barnard (2001), Influence of surface waves on measured and modeled irradiance profiles, *Appl. Opt.*, *40*(9), 1442–1449.